



Adaptive Control of a Tendon-Driven Manipulator for Capturing Non-Cooperative Space Targets

Justin E. Kernot* and Steve Ulrich†
Carleton University, Ottawa, Ontario K1S 5B6, Canada

<https://doi.org/10.2514/1.A34881>

Orbital debris in Earth orbit poses a threat to the future of spaceflight. To combat this issue, this paper proposes a novel robotic mechanism for non-cooperative capture and active servicing missions on non-cooperative targets; specifically, a tendon-driven manipulator is assumed for this work. The capture mechanism is a prototype symmetric two-link gripper driven by an open-ended cable-sheath transmission mechanism. Because the cable-sheath transmission mechanism is a nonlinear time-varying hysteretic system, two separate adaptive control strategies were compared against the uncontrolled and proportional-integral-derivative controlled performance of the closed-loop gripper. Specifically, an indirect control method and a direct \mathcal{L}_1 controller were employed. Experimental results demonstrate that the adaptive controllers show better tracking performance of a joint trajectory over the proportional-integral-derivative controlled and uncontrolled cases, whereas the \mathcal{L}_1 controller performs best under dynamic conditions, and the indirect controller performs best in steady state.

I. Introduction

AS SLOW Earth orbits (LEOs) continue to be populated, there is an ever-increasing risk of collision between active spacecraft and orbital debris. In fact, there are nearly 19,000 catalogued objects over 10 cm in diameter that populate the orbital environment [1], including spent upper stages, fragmented debris, and nonoperational spacecraft. Kessler demonstrated that this number will continue to grow exponentially as per the Kessler syndrome, which can be described as the perpetuated fragmentation of orbital objects through cascading collisions [2]. Even with no new launches, some models predict that the debris density will increase by a factor of approximately 2.4 in LEO within a 200-year period [3]. If no action is taken, the future of spacecraft operations will undoubtedly be negatively impacted by higher costs and potential loss of entire missions [4].

Despite these alarming results, the European Space Agency (ESA) reported that removing as little as five large objects per year from the orbital environment would mitigate this unstable growth [5]. This can be accomplished through active debris removal missions, or by performing on-orbit servicing missions to extend the operation of existing satellites, thereby reducing the frequency of spacecraft launches. As a result, several space agencies (NASA, ESA, Canadian Space Agency [CSA], and Japan Aerospace Exploration Agency [JAXA]) are currently working on solutions to these problems to prevent the orbital environment from becoming inaccessible.

The capture of an inactive satellite in orbit poses several challenges, as the target is considered “non-cooperative.” Because the target may not be under its own control, or have a prescribed capture interface on the target, the servicing spacecraft must perform a capture maneuver that can overcome these problems. The preferred solution to this problem would be to employ a capture mechanism that can accommodate a wide number of target geometries to ensure a rigid capture is made. Several capture strategies exist that have been proven to perform well under prescribed operating conditions; however, it becomes increasingly challenging to ensure that the servicing

manipulator can perform unexpected tasks as they arise during the mission.

There have been numerous solutions proposed to address the orbital capture problem. Generally, this problem is divided into two primary subsets: flexible capture and rigid capture [6,7]. To enable manipulation tasks for on-orbit servicing missions and orbital debris removal, a rigid capture between the servicing craft and target is often preferred. Because a rigid connection can be accomplished only with a robotic manipulator, it is this subset of capture devices that are of key interest. In general, these robotic capture mechanisms can be applied to two mission scenarios: cooperative capture and non-cooperative capture. Cooperative targets are under full control and have a predefined capture interface for the servicing craft to latch onto. Examples of flight-proven cooperative capture interfaces include the advanced robotics hand onboard the ETS-VII space robot system [8], the widely known latching end-effector (LEE) currently used on the Space Station Remote Manipulator System (SSRMS) [9], the manipulation tools used on the Canadian Special Purpose Dexterous Manipulator robot during the Robotic Refueling mission (RRM) [10], and the orbital-express (OE) capture mechanism [11,12]. For servicing missions in geostationary orbit (GEO), efforts are being made by ESA to develop a standardized cooperative docking/berthing interface by making use of a pantographic probe and berthing cone [13]. On a smaller scale, examples of cooperative capture interfaces are in abundance in experimental testbeds, including the mating-cone-type capture mechanism employed by the POS-EIDYN air-bearing facilities at Naval Postgraduate School (NPS) [14], and the mechanical capture interface employed by the free-floating SPHERES/Astrobee platforms [15].

With non-cooperative targets, the object of interest is under no control of its own and does not have a predefined capture interface. To accomplish the capture of non-cooperative targets, several robotic strategies have been considered. The Phoenix program is an initiative developed by the Defense Advanced Research Projects Agency (DARPA) and U.S. Naval Research Laboratory (NRL) to test technologies and strategies to validate their applicability for servicing missions, such as repairing decommissioned spacecraft or debris removal in geostationary equatorial orbit (GEO) [16]. One example of an on-orbit demonstration is the testing of the Front-end Robotics Enabling Near-term Demonstration (FRIEND) arm equipped with a basic clamping capture tool to perform a robotic assembly of external payload, and a series of dexterous manipulation tasks [17]. Additionally, ESA’s e. Deorbit mission plans to launch several debris removal technologies, including a clamp-type robotic gripper mechanism [18]. Another example of a robotic clamping mechanism is the Launch Adapter Ring (LAR) Capture Tool developed by MacDonald, Dettwiler and Associates (MDA). The LAR capture tool employs a robotic clamping mechanism that latches to the launch adapter ring

Presented as Paper 2020-2080 at the AIAA Scitech 2020 Forum, Orlando, FL, January 6–10, 2020; received 15 June 2020; revision received 22 April 2021; accepted for publication 23 April 2021; published online 16 July 2021. Copyright © 2021 by Justin Kernot and Steve Ulrich. Published by the American Institute of Aeronautics and Astronautics, Inc., with permission. All requests for copying and permission to reprint should be submitted to CCC at www.copyright.com; employ the eISSN 1533-6794 to initiate your request. See also AIAA Rights and Permissions www.aiaa.org/randp.

*Graduate Student, Department of Mechanical and Aerospace Engineering, 1125 Colonel By Drive.

†Associate Professor, Department of Mechanical and Aerospace Engineering, 1125 Colonel By Drive. Senior Member AIAA.

of unprepared targets [19]. A similar solution developed by OHB specifically for capturing Envisat also makes use of capturing a LAR interface through mechanical clamping mechanisms [20]. Although this method is suitable for targets that possess a launch adapter ring, as shown experimentally by Oleš et al. on the microgravity simulator at the Space Research Centre of the Polish Academy of Sciences [21], it cannot perform a rigid capture if this interface does not exist. Another approach to robotic capture is to envelop the target with a continuum manipulator. An example of this technology is the “tentacle”-type gripper developed for the CleanSpace One mission. Equipped with four dielectric elastomer minimum energy structures (DEMES) acting as the links, this mechanism is designed to capture a nanoscale satellite by entirely enveloping the target [22]. This concept, though lightweight and universal, cannot be scaled up to larger spacecraft due to its low rigidity and retention force limits.

Another possible solution for the rigid capture of non-cooperative targets is to employ a tendon-driven manipulator. A tendon-driven manipulator is a robotic device in which the joints are controlled by cables in tension connected to actuators located distally from the joints [23–25]. Li et al. [26] demonstrated the effectiveness of this type of manipulator by modeling a four-link underactuated serial tendon-driven manipulator on a free-floating spacecraft and simulated its set-point tracking performance using a proportional-derivative controller. This type of manipulator has several advantages over conventional robotic manipulators. The first is that an end-effector (EE) driven by such a mechanism would have a lower mass because there are no actuators located at the joints, resulting in better endpoint response. Furthermore, a large torque can be generated for a smaller manipulator because the actuators can be much larger than those required to fit within volumetric constraints of a robotic joint. Aside from these benefits, however, there are several challenges associated with routing the tendons from the actuators to the joints. There are two main routing methods. The first is a pulley routing system, whereby the tendon (or driving cable) is routed through a series of pulleys [27,28]. This routing method offers reduced transmission losses at the expense of greatly increasing the complexity and size of the manipulator. The other primary form of tendon transmission is the use of a cable-sheath transmission mechanism (CSTM), where the driving tendons are routed through a flexible conduit from the actuating mechanism to the joint [29–31]. The CSTM offers several benefits over the pulley configuration by reducing mass, volume, and complexity while increasing its flexibility. The main issue with the CSTM is that it introduces nonnegligible hysteretic friction between the cable and sheath, dead zones, and backlash nonlinearities that vary with the curvature configuration of the sheath.

There have been numerous models proposed to identify and mitigate these nonlinearities. Kaneko et al. [31,32] were among the first researchers to develop a CSTM model that was based on Coulomb friction and lumped mass theory. In this work, it was assumed that the CSTM maintains a fixed curvature and that the cable is always under sufficient pretension. Palli and Melchiorri [33] and Palli et al. [34] then extended this research by considering the effects of the Dahl friction model on the CSTM and proposed a compensation strategy based on tension feedback to mitigate the effects of friction. Palli and Melchiorri [35] further improved upon his work by developing an optimal control strategy, which further improved the CSTM compensation. However, Palli’s compensation strategy greatly increased the number of tendon elements required in the model, which led to an increase in computational requirements. In response to these complications, Agrawal et al. [36] used a general piecewise differential backlash model to develop an inverse-feed-forward control scheme that was used to effectively improve the position tracking error of the output. In a similar fashion, both Kesner and Howe [37] and Reilink et al. [38] used an inverse backlash model as a control strategy for a known and fixed CSTM configuration. The methods proposed in these works use a switching function for the velocity of the tendon elements, which unfortunately introduces discontinuities in the compensator. Xu and Simaan [39], Xu et al. [40], and Xu and Simaan [41] used an inverse kinematics compensation approach, which required knowledge of the joint states of a continuum robot. Unfortunately, all of these proposed strategies

operate under the assumption that the model parameters are known. In practice, this is an unrealistic assumption because the configuration and hysteresis characteristics of the sheath will change as the manipulator is actuated.

To account for a time-varying CSTM configuration, several indirect adaptive control strategies have been developed. Wang et al. [42] explored the adaptive control for a class of continuous-time nonlinear dynamic systems with an unknown dead zone. Guo et al. [43] built upon this work by redefining a set of projection-based adaptation laws, and Hu et al. [44] proposed an integrated direct/indirect adaptive robust control scheme based on a dead-zone model. The adaptive control strategies proposed in these works all used the same dead-zone model used by Tao and Kokotovic [45]. A consequence of this model is that it is discontinuous, which can result in unwanted tracking characteristics. In response, Do et al. [46] developed a continuous model based on a modification to the asymmetric Bouc–Wen hysteresis model, and then proposed an indirect adaptive control strategy [47,48] that uses parameter adaptation laws based on this model. This control strategy has been shown to yield among the best results for position tracking in robotic CSTM systems while having the capability of operating under dynamic conditions. However, the indirect adaptive controller by Do et al. [47,48] has only been applied to a single, isolated CSTM system, as opposed to a functional multilink system. Furthermore, a downside to this form of adaptive control is that it is indirect, implying that it still requires a system dynamics model. Because it is nearly impossible to perfectly match such a complex system to an analytical model, there will always be discrepancies between the model and the real system.

Conversely, direct adaptive control methods do not require explicit parameter identification and are well-suited for a wide class of multiple-input–multiple-output systems subjected to significant uncertainties and disturbances [49]. As such, a direct adaptive controller would be preferred for the control of a time-varying system with little or no prior knowledge of the plant. A suitable candidate for this control problem would be the \mathcal{L}_1 adaptive controller as it has been shown to perform well to hysteretic systems. Zou et al. [50] and Fan and Smith [51] showed in simulation that the \mathcal{L}_1 controller could achieve stable tracking for uncertain systems in the presence of time-varying and state-dependent unknown nonlinear hysteresis. Furthermore, Zhang et al. [52] demonstrated superior tracking performance in an experiment of a hysteretic piezoelectric actuator when compared with more traditional control schemes. Additionally, a more complex \mathcal{L}_1 control scheme with the inclusion of a fuzzy-logic component was applied to generic systems with an unknown backlash-like hysteresis by Yousef et al. [53] in a simulated environment, and they demonstrated its effectiveness. To the best of the author’s knowledge, the \mathcal{L}_1 method of control has not yet been applied specifically to a CSTM experimentally.

In this context, the main original contributions of this work are 1) the development of a direct adaptive control methodology for a CSTM capture mechanism designed for the rigid capture of a non-cooperative space target, based the \mathcal{L}_1 adaptive control theory; 2) the extension of the indirect controller by Do et al. [47,48] originally developed for a single, isolated CSTM system, to a functional multilink tendon-driven robotic system; and 3) the experimental validation of both adaptive control strategies on a multilink tendon-driven CSTM gripper prototype developed for use on the Spacecraft Proximity Operations Testbed (SPOT) at Carleton University’s Spacecraft Robotics and Control Laboratory (SRCL). The purpose for developing the capture mechanism to function on the SPOT platform is to enable the capability of future experiments in a free-floating environment. Furthermore, the performance of the capture mechanism under the \mathcal{L}_1 adaptive control and the multilink indirect adaptive scheme will be compared against a no control case and a simple proportional-integral-derivative (PID) control scheme under several fixed and time-varying configurations.

In Sec. II, a general overview of the tendon-driven manipulator and a description of the closed-loop system are provided. The following two sections provide the theory of the adaptive controllers selected for this work, where Sec. III covers the indirect adaptive control law developed by Do et al. [47,48], and Sec. IV covers the proposed

\mathcal{L}_1 -based direct adaptive control scheme. Section V then shows the development of the prototype tendon-driven manipulator and its tracking performance for the four control cases selected. Finally, Sec. VI concludes this work by summarizing the key results and provided a brief note on practicality.

II. System Description

This section describes the general concept of the tendon-driven manipulator developed in this work to give context for the selected adaptive control schemes covered in later sections. Then, a kinematic model is presented that describes the input-to-output relationship of a CSTM for a given position command, followed by the generalized control strategy of the capture mechanism.

A. Tendon-Driven Manipulator Concept

Based on the literature, there are several possible joint configurations for a tendon-driven manipulator. One common method involves fully rigidizing the joint by coupling an antagonistic pair of cables routed through independent sheaths [24,27,28,31]. This method has the advantage of ensuring that the joints are stiff and that there is actuated control in both operating directions. However, this type of strategy doubles the amount of required hardware, is more complicated to install with the correct pretension, and requires a pulley to function. Because the mechanism of interest only requires a clamping force in one direction, this solution would add cost, complexity, and mass to the project.

Conversely, there exists an open-ended design that employs a single antagonistic tendon in the direction of operation, and a spring to provide a restitution torque in the opening direction when the cable is slackened [23,27,54]. This method offers a great degree of flexibility in the design process as it simplifies a number of challenges associated with dual antagonistic methods. For instance, the use of a spring will ensure that the cable is in sufficient pretension at all times of its operation, while reducing the complexity and cost of the system. This configuration was selected due to the advantages that the open-ended single tendon design has in the context of this work.

An uncommon subset of this type of CSTM joint is one that does not employ a pulley at the joint. The use of the pulley is primarily used to maintain a constant torque arm at the joint and to ensure that the tendon is routed properly. Because the volumetric form factor of the experiment is restricted and the joints must be kept simplistic in their design, it was deemed most appropriate to select the joint type with no pulley. Thus, the selected joint configuration is highlighted in Fig. 1, where the key components are labeled.

Each link of the capture mechanism is controlled by its own CSTM connected to a servomotor that is distally located from the joints of the manipulator. When a torque is generated by the servomotor, the winch pulley will generate a tension at the input end of the sheath, which will result in a reaction at the output end. The output tension generated by the cable induces a torque on the manipulator links in the closing direction to apply a clamping force. The torsion springs at each joint produce a torque in the opposite direction to maintain pretension in the cable. When the actuators release the tension in the cables, the torsion springs provide a restitution force in the opening direction of the capture mechanism to return to its neutral position.

B. CSTM Kinematic Model

The interaction between the cable and sheath of a CSTM can be modeled in two ways: through a dynamic model or through a kinematic model. For reasons that will become clearer in the following section, it was deemed more appropriate to describe the system in terms of a kinematic model. Do et al. [46], showed that any CSTM can be defined by using a nonlinear backlash hysteresis model for a fixed sheath configuration (or curvature). This model was adapted from the generalized asymmetric Bouc–Wen model developed by Song and Der Kiureghian [55], which was optimized for computational efficiency by reducing the number of nonlinear parameters while giving it a continuous form. This model is able to determine the output position of a fixed CSTM configuration given the position and velocity of the tendon at the input end of the sheath. The model is given by

$$x_{out}(t) = \alpha_x(\dot{x}_{in}(t))x_{in}(t) + \zeta(t) \quad (1)$$

where x_{in} represents the position of the tendon at the input and x_{out} represents the position of the tendon at the output end of the sheath. In this expression, the function $\alpha_x(\dot{x}_{in}(t))$ is a smooth transition function between loading and unloading phases of the hysteresis loop, and $\zeta(t)$ is the internal state variable of the CSTM. These parameters can be determined by the following equations:

$$\alpha_x(\dot{x}_{in}(t)) = \frac{\alpha_1 e^{2\dot{x}_{in}(t)} + \alpha_2}{e^{2\dot{x}_{in}(t)} + 1} \quad (2)$$

$$\dot{\zeta}(t) = A\dot{x}_{in}(t) - \nu|\dot{x}_{in}(t)|\zeta(t) + \delta|\dot{x}_{in}(t)| \quad (3)$$

where the parameters $\alpha_1 > 0$, $\alpha_2 > 0$, A , ν , and δ are all constant parameters that control the shape of the hysteresis loop for a fixed

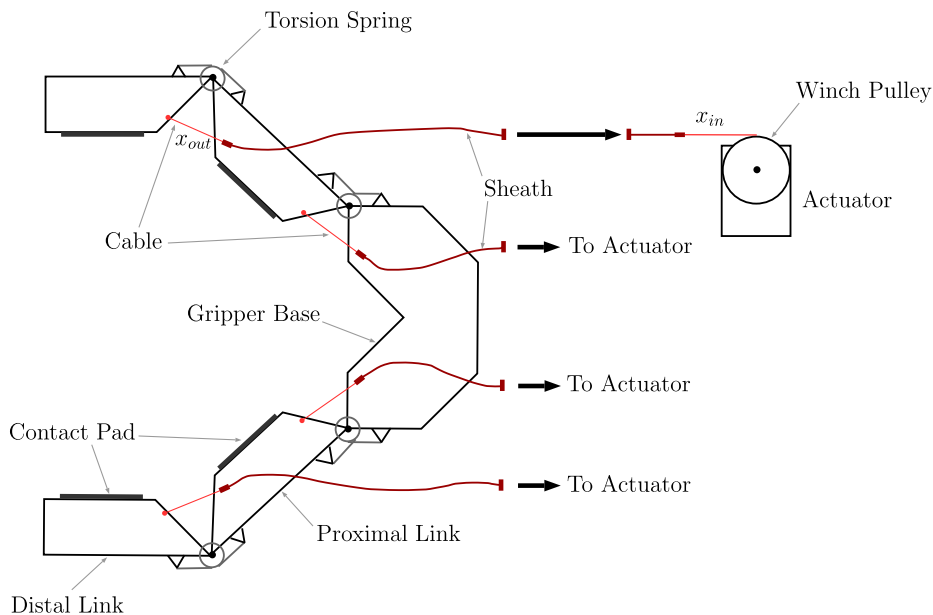


Fig. 1 Selected joint configuration for the capture mechanism.

configuration. In practice, these parameters would be determined for a single configuration of the CSTM by recording experimental data and performing any form of parameter estimation technique (i.e., optimization routine, genetic algorithm, etc.) to return the model values that best fit the data. Note that the model presented by Eqs. (1–3) assumes that the cable remains in tension at all times (i.e., it does not slacken).

A simulated example of Eq. (1) can be seen in Fig. 2, where the tracking performance, error, and hysteresis loop are simulated for a rotational joint controlled by a CSTM. The parameters used in this simulation were taken from the experimental CSTM used by Do et al. [46] and are listed as follows: $\alpha_1 = 0.8972$, $\alpha_2 = 0.9487$, $A = -0.8745$, $\nu = 5.034$, and $\delta = 0.1452$.

Because the manipulator proposed in this paper will not have a fixed CSTM configuration during a maneuver (as was the case in Fig. 2), the model parameters $\alpha_1 > 0$, $\alpha_2 > 0$, A , ν , and δ will vary as a function of time. This poses a problem for controlling the system because the relationship between the input and output of the sheath will be undefined as the CSTM configuration changes.

C. Control Objective

Before developing an appropriate control strategy to address the dynamic characteristics of a CSTM, let us first review the control objectives for the manipulator. First, we define the states of each joint to be the angular position and velocity of each individual link.

$$\mathbf{x}_i = \begin{bmatrix} \theta_i \\ \dot{\theta}_i \end{bmatrix} \quad (4)$$

where \mathbf{x}_i and θ_i denote the state vector and the angular position of link i , respectively. Because each link is controlled by an independent actuator with its own CSTM and unique joint geometry, it was deemed appropriate to implement an individual control loop for each joint separately. The general control loop for a given joint is presented by Fig. 3, where $\mathbf{u}(t)$ is the feedback control signal sent to the servomotor driving the CSTM connected to a given joint.

The exact control architecture may change based on the control algorithms selected. However, the principle of the control objective will remain the same: to implement a state-feedback-type controller to command a desired joint angle trajectory.

As mentioned previously, controlling a CSTM presents a challenge due to time-varying friction and backlash hysteresis that is present in the system. Because of these characteristics, the set point tracking accuracy for a fixed controller would vary with the CSTM configuration during a manipulation task. To address this issue, this paper proposes two adaptive control strategies to compare against the uncontrolled case and a standard fixed-gain PID controller: the

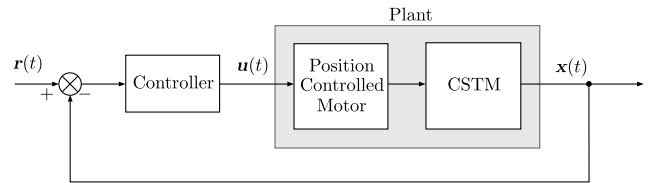


Fig. 3 General control architecture for the CSTM-driven manipulator.

indirect controller developed for CSTMs by Do et al. [47,48], herein extended to a multilink tendon-driven manipulator, and the novel \mathcal{L}_1 -based direct adaptive controller.

III. Indirect Adaptive Control of CSTMs

In general terms, an indirect adaptive control scheme is one that requires an accurate mathematical model of the system that is being controlled. Using this knowledge, a set of adaptive laws is developed, which is used to estimate the parameters associated to the selected model. Do et al. [47,48] made use of this method to develop a control strategy based on the modified Bouc–Wen model covered in the previous section.

To develop this control algorithm (hereinafter referred to as the indirect adaptive controller), the definition of variables can be restructured as a controlled system by recognizing that $x_{in}(t)$ from Eq. (1) can be considered as the control input $u(t)$ to the plant. Additionally, an unknown disturbance $d(t)$ can be introduced to Eq. (1) to represent a sudden configuration change to the CSTM. Thus, the system model is redefined as

$$\Phi(t) = \alpha_x(\dot{u}(t))u(t) + \zeta(t) + d(t) \quad (5)$$

$$= \alpha_x(\dot{u}(t))u(t) + \Delta_n(t) \quad (6)$$

where $\Phi(t)$ is the output of the system and $\Delta_n(t)$ is the internal state $\zeta(t)$ combined with the disturbance $d(t)$ bounded by a positive $\Delta_n^*(t)$. Before the indirect adaptive control algorithm is developed, the following assumptions must be made: 1) the cable is under tension at all times, and 2) the exact model parameters of the CSTM and their bounds are unknown and are not required for the operation of the controller.

The objective of the controller is to have $\Phi(t)$ track a known reference position signal $x_r(t)$, where the tracking error between them is defined to be $e_r(t) = \Phi(t) - x_r(t)$. With this definition, the following coordinate transformations for Eq. (6) can be defined as

$$n(t) = \int_0^t e_r(\tau) d\tau \quad (7)$$

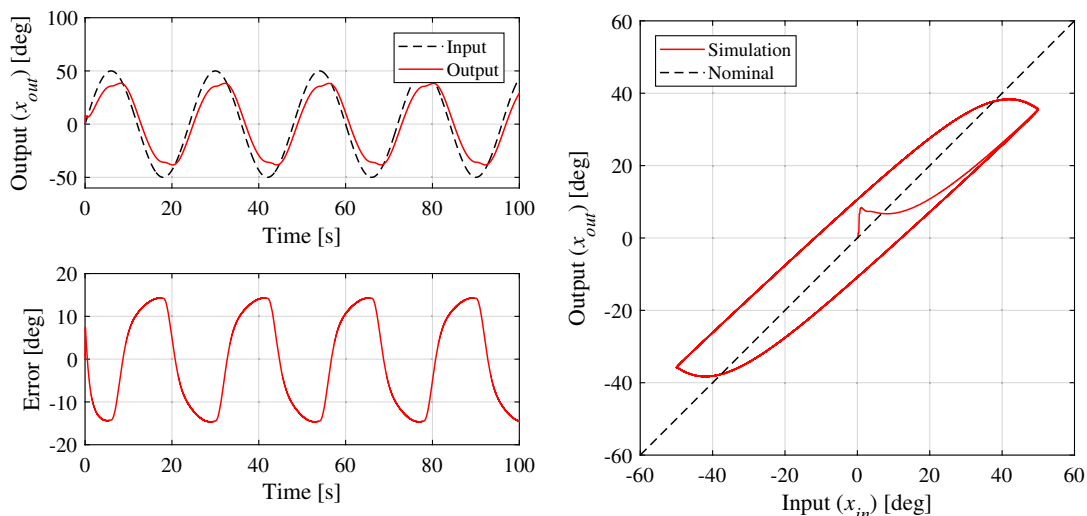


Fig. 2 CSTM output tracking performance given an angular input position. Top: position at the input of the sheath and the output of the sheath. Bottom: error between input and output. Right: hysteresis loop.

$$\omega(t) = e_r(t) + \alpha n(t) \quad (8)$$

where $n(t)$ is the cumulative integral of the tracking error (or error history), α is a user-defined scaling factor, and $\omega(t)$ is a linear combination of the error and its integral. Therefore, $\omega(t)$ is analogous to a proportional-integral controller applied to the error signal of the system. By taking the derivative of this term and by making use of Eqs. (2), (6), and (8), $\dot{\omega}(t)$ can be rewritten as follows:

$$\dot{\omega}(t) = \alpha e_r(t) + \dot{e}_r(t) \quad (9)$$

$$\dot{\omega}(t) = \alpha \left[\left(\frac{\alpha_1 e^{2\hat{u}(t)} + \alpha_2}{e^{2\hat{u}(t)} + 1} \right) u(t) + \Delta_n(t) - x_r(t) \right] + \dot{e}_r(t) \quad (10)$$

To simplify the controller design, $u(t)$ can be defined as the linear combination of two separate controllers $u_1(t)$ and $u_2(t)$ such that Eq. (11) is valid:

$$u(t) = u_1(t) + u_2(t) \quad (11)$$

where $u_1(t)$ and $u_2(t)$ are defined as follows:

$$u_1(t) \triangleq \frac{u(t) e^{2\hat{u}(t)}}{e^{2\hat{u}(t)} + 1} \quad (12)$$

$$u_2(t) \triangleq \frac{u(t)}{e^{2\hat{u}(t)} + 1} \quad (13)$$

Note that Eqs. (12) and (13) do not depend on one another. Upon careful inspection, one can conclude that the term in Eq. (10) due to $\alpha_x(\dot{u}(t))u(t)$ is equivalent to the linear combination of $u_1(t)$ and $u_2(t)$, which is demonstrated below:

$$\alpha_1 u_1(t) + \alpha_2 u_2(t) = \frac{\alpha_1 e^{2\hat{u}(t)} + \alpha_2}{e^{2\hat{u}(t)} + 1} u(t) \quad (14)$$

Combining Eq. (14) reduces Eq. (10) to the following simpler form:

$$\dot{\omega}(t) = \alpha[\alpha_1 u_1(t) + \alpha_2 u_2(t) + \Delta_n(t) - x_r(t)] + \dot{e}_r(t) \quad (15)$$

For later convenience, let χ_i ($i = 1, 2$) be the inverse of α_i , and let $\Delta_n(t)$ be redefined in terms of its boundary $\Delta_n^*(t)$, as provided in Eq. (16).

$$\Delta_n(t) = \tanh\left(\frac{\omega(t)}{\epsilon}\right) \Delta_n^*(t) \quad (16)$$

By substituting these definitions back into Eq. (15), the expression for $\dot{\omega}(t)$ becomes the following:

$$\dot{\omega}(t) = \alpha \left[\frac{1}{\chi_1} u_1(t) + \frac{1}{\chi_2} u_2(t) + \tanh\left(\frac{\omega(t)}{\epsilon}\right) \Delta_n^*(t) - x_r(t) \right] + \dot{e}_r(t) \quad (17)$$

Since χ_1, χ_2 , and $\Delta_n^*(t)$ are unknown, they are replaced with their respective estimated parameters: $\hat{\chi}_1, \hat{\chi}_2$, and $\hat{\Delta}_n^*(t)$, which are assumed to be ideal.

$$\dot{\omega}(t) = \alpha \left[\frac{1}{\hat{\chi}_1} u_1(t) + \frac{1}{\hat{\chi}_2} u_2(t) + \tanh\left(\frac{\omega(t)}{\epsilon}\right) \hat{\Delta}_n^*(t) - x_r(t) \right] + \dot{e}_r(t) \quad (18)$$

Equation (18) is then further simplified by expressing $u_i(t)$ in terms of virtual controllers $\bar{u}_i(t)$, where by definition $u_i(t) = \hat{\chi}_i \bar{u}_i(t)$.

$$\dot{\omega}(t) = \alpha \left[\bar{u}_1(t) + \bar{u}_2(t) + \tanh\left(\frac{\omega(t)}{\epsilon}\right) \hat{\Delta}_n^*(t) - x_r(t) \right] + \dot{e}_r(t) \quad (19)$$

Since $\dot{\omega}(t)$ is related to the error signal $e_r(t)$, \bar{u}_i is selected such that Eq. (19) can be expressed in a similar form to Eq. (9) while canceling out unnecessary terms. Therefore, the virtual controllers are designed as per the following expressions:

$$\bar{u}_1(t) = -k_1 \omega(t) - \tanh\left(\frac{\omega(t)}{\epsilon}\right) \hat{\Delta}_n^*(t) + x_r(t) - \frac{1}{\alpha} \dot{e}_r(t) \quad (20)$$

$$\bar{u}_2(t) = -k_2 \omega(t) \quad (21)$$

where k_1 and k_2 are positive proportional constants used to control the weight of each virtual controller. Recalling the definition of $u(t)$ from Eq. (11), the final form of the controller can be constructed as per Eq. (22). Note that $\hat{\chi}_i$ will vary with time for a changing CSTM configuration.

$$u(t) = \hat{\chi}_1(t) \bar{u}_1(t) + \hat{\chi}_2(t) \bar{u}_2(t) \quad (22)$$

The adaptive laws to determine the estimated parameters $\hat{\chi}_1(t)$, $\hat{\chi}_2(t)$, and $\hat{\Delta}_n^*(t)$ are given in Eqs. (23–25), where δ_i is a user-specified positive constant to control the adaptation rate, and σ_i is a small positive constant used to prevent the estimated parameters from diverging to large values.

$$\dot{\hat{\chi}}_1(t) = -\delta_1 \bar{u}_1(t) \omega(t) - \sigma_1 \hat{\chi}_1(t) \quad (23)$$

$$\dot{\hat{\chi}}_2(t) = -\delta_2 \bar{u}_2(t) \omega(t) - \sigma_2 \hat{\chi}_2(t) \quad (24)$$

$$\dot{\hat{\Delta}}_n^*(t) = \delta_3 \omega(t) \tanh\left(\frac{\omega(t)}{\epsilon}\right) - \sigma_3 \hat{\Delta}_n^*(t) \quad (25)$$

Theorem 1: Consider the nonlinear system outlined in Eq. (10) and the adaptive controller given by Eqs. (20–25).

1) The position tracking error $e_r(t)$ and the adaptive parameters $\hat{\chi}_1(t)$, $\hat{\chi}_2(t)$, and $\hat{\Delta}_n^*(t)$ are uniformly ultimately bounded in the closed-loop system.

2) The position tracking error $e_r(t)$ converges to a desired compact region in the presence of unknown model parameters.

Proof: Please refer to the work of Do et al. [47,48] for the Lyapunov stability proof of this theorem. \square

IV. \mathcal{L}_1 Control with Hysteresis Compensation

There are several direct adaptive \mathcal{L}_1 control strategies available in literature that have been shown to be effective for many types of systems. For example, Dodenhöft et al. applied an augmented \mathcal{L}_1 controller to NASA's Transport Class Model [56]. Jafarnejadsani et al. demonstrated its application for sampled-data control for uncertain multi-input–multi-output (MIMO) systems [57], and Nayyeri et al. provided an optimal tuning strategy for an inverted pendulum system [58]. In the case of a system with hysteresis, such as the implemented CSTM, it has been shown by multiple authors that the \mathcal{L}_1 controller with a state predictor and uncertain input gains is an appropriate choice [50–52]. This section covers the system transformation of the CSTM to account for hysteresis, the development of the companion model adaptive controller (CMAC) with a state predictor, and the modification of the CMAC architecture into the \mathcal{L}_1 control architecture to be employed to the system.

A. System Transformation

In CMAC control, it is necessary that the plant is a linear time-invariant, single-input–single-output (SISO) system governed by the following state space formulation:

$$\dot{\mathbf{x}}(t) = \mathbf{A}\mathbf{x}(t) + \mathbf{B}\mathbf{u}(t) \quad (26)$$

$$\mathbf{y}(t) = \mathbf{C}\mathbf{x}(t) \quad (27)$$

where $\mathbf{x}(t)$ represents the $n \times 1$ state vector of the system, $\mathbf{u}(t)$ is the $m \times 1$ control input, $\mathbf{y}(t)$ is the output of the system (typically with a dimension of 1×1), \mathbf{A} is the $n \times n$ system matrix, and \mathbf{B} is the $n \times m$ control matrix. However, because CSTM systems are highly nonlinear hysteretic systems, their dynamics do not follow Eqs. (26) and (27). Fortunately, it has been demonstrated that nonlinear hysteretic systems can be controlled with a modified \mathcal{L}_1 control architecture, where the hysteresis nonlinearities are treated as an uncertain system input gain [50–52,59]. This can be shown graphically in Fig. 4 as a decoupled system with the hysteresis transformation occurring before the plant.

where the signal $\omega(t)$ is the transformed control signal, and $\sigma_d(t)$ is a vector of bounded disturbances such as noise and other perturbations. By applying these signals to the definition of the dynamics presented by Eq. (26), the system dynamics can then be rewritten as

$$\dot{\mathbf{x}}(t) = \mathbf{A}\mathbf{x}(t) + \mathbf{B}(\omega_u(t) + \sigma_d(t)) \quad (28)$$

The hysteresis transformation $\omega_u(t)$ is found by applying Eq. (29) to the bounded control signal $\mathbf{u}(t)$.

$$\omega_u(t) = \gamma(t)\mathbf{u}(t) + \sigma_u(t) \quad (29)$$

where the definitions of $\gamma(t)$ and $\sigma_u(t)$ are best described by referring to the graphical representation of the hysteresis transformation shown in Fig. 5 below, where $\omega_u(t)$ and $\mathbf{u}(t)$ are mapped to the vertical and horizontal axes, respectively.

By substituting Eq. (29) into Eq. (28), and by defining $\sigma(t) = \sigma_d(t) + \sigma_u(t)$, the state equation of the system can be found as follows:

$$\dot{\mathbf{x}}(t) = \mathbf{A}\mathbf{x}(t) + \mathbf{B}(\gamma(t)\mathbf{u}(t) + \sigma(t)) \quad (30)$$

For a real system, it can be assumed that the parameters $\gamma(t)$ and $\sigma(t)$ are uniformly bounded, and that there is partial knowledge of the system, as

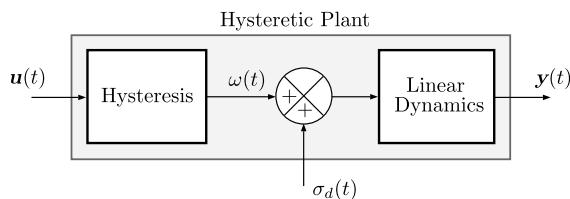


Fig. 4 Decoupled hysteresis model and plant for nonlinear system.

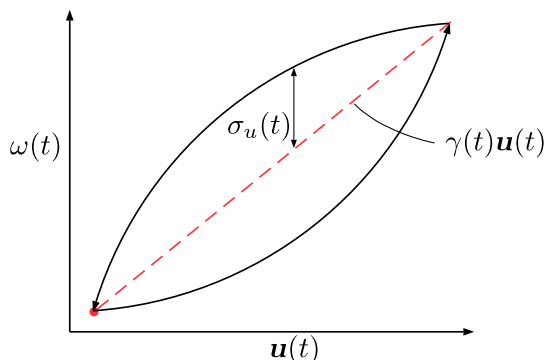


Fig. 5 Graphical representation of the nonlinear transformation applied to the system input $\mathbf{u}(t)$.

$$\gamma(t) \in \Upsilon_0 \triangleq [\gamma_l, \gamma_u] \quad (31)$$

$$|\sigma(t)| \leq \Delta_o \quad \forall t \geq 0 \quad (32)$$

where $0 \leq \gamma_l \leq \gamma_u$, and Δ_o are known/user-defined constants that define the conservative bounds for their respective parameters.

B. CMAC Architecture

Now that the system to be controlled has been defined, let us define a control objective based on the standard CMAC architecture. At its most fundamental level, the control objective of CMAC is to design an adaptive feedback control signal $\mathbf{u}(t)$ that minimizes the error between the output of the system $\mathbf{y}(t)$ and a user-defined reference dynamics model. The reference model that determines the desired closed-loop dynamics is given as

$$\dot{\mathbf{x}}_m(t) = \mathbf{A}_m\mathbf{x}_m(t) + \mathbf{B}k_g\mathbf{r}(t) \quad (33)$$

$$\mathbf{y}_m(t) = \mathbf{C}\mathbf{x}_m(t) \quad (34)$$

In this model, \mathbf{A}_m is a known Hurwitz matrix of the desired dynamics defined by the user, \mathbf{B} is the control matrix of the system, and $\mathbf{r}(t)$ is the reference signal known a priori. The matrix \mathbf{A}_m is considered Hurwitz if and only if every eigenvalue of \mathbf{A}_m has a strictly negative real part. The scalar k_g is defined by

$$k_g \triangleq -\frac{1}{\mathbf{C}\mathbf{A}_m^{-1}\mathbf{B}} \quad (35)$$

such that the output of the system will converge to the reference signal as $t \rightarrow \infty$. By definition, the relationship to the actual system matrix \mathbf{A} and the companion matrix \mathbf{A}_m is defined by

$$\mathbf{A} \triangleq \mathbf{A}_m + \mathbf{B}\boldsymbol{\theta}(t)^T \quad (36)$$

where $\boldsymbol{\theta}(t) = [\theta_1, \dots, \theta_n]^T$ is a set of unknown parameters assumed to be uniformly bounded and belonging to the convex compact set $\boldsymbol{\theta}(t) \in \Theta$. The system matrix \mathbf{A} outlined previously in Eq. (30) is typically unknown. However, with the relationship given in Eq. (36), the system can now be more conveniently expressed in terms of the companion matrix \mathbf{A}_m , as shown below:

$$\dot{\mathbf{x}}(t) = \mathbf{A}_m\mathbf{x}(t) + \mathbf{B}(\gamma(t)\mathbf{u}(t) + \boldsymbol{\theta}(t)^T\mathbf{x}(t) + \sigma(t)) \quad (37)$$

By assuming the same form of the redefined system model in Eq. (37), the state predictor is defined as

$$\dot{\hat{\mathbf{x}}}(t) = \mathbf{A}_m\hat{\mathbf{x}}(t) + \mathbf{B}(\hat{\gamma}(t)\mathbf{u}(t) + \hat{\boldsymbol{\theta}}(t)^T\mathbf{x}(t) + \hat{\sigma}(t)) \quad (38)$$

where the unknown parameters are replaced with their estimated values, $\hat{\gamma}(t)$, $\hat{\boldsymbol{\theta}}(t)$, and $\hat{\sigma}(t)$, accordingly. The projection adaptation laws used to govern the estimated parameters are given by

$$\dot{\hat{\gamma}}(t) = \Gamma \text{Proj}(\dot{\hat{\gamma}}(t), -\tilde{\mathbf{x}}(t)\mathbf{P}\mathbf{B}\mathbf{u}(t)) \quad (39)$$

$$\dot{\hat{\boldsymbol{\theta}}}(t) = \Gamma \text{Proj}(\dot{\hat{\boldsymbol{\theta}}}(t), -\tilde{\mathbf{x}}(t)\mathbf{P}\mathbf{B}\mathbf{x}(t)) \quad (40)$$

$$\dot{\hat{\sigma}}(t) = \Gamma \text{Proj}(\dot{\hat{\sigma}}(t), -\tilde{\mathbf{x}}(t)\mathbf{P}\mathbf{B}) \quad (41)$$

where $\tilde{\mathbf{x}}(t) = \hat{\mathbf{x}}(t) - \mathbf{x}(t)$ is the parametric estimation error dynamics by definition. In these adaptive laws, Γ is the learning rate of the control algorithm, and the matrix $\mathbf{P} = \mathbf{P}^T > 0$ is the solution to the Lyapunov equation $\mathbf{A}_m^T\mathbf{P} + \mathbf{P}\mathbf{A}_m = -\mathbf{Q}$ for an arbitrary $\mathbf{Q} = \mathbf{Q}^T > 0$. The projection operation used in these adaptation laws is outlined by Hovakimyan and Cao [59].

With this information, a nominal controller $\mathbf{u}_n(t)$ can be defined such that the effects of the unknown parameters are canceled out, and such that the system dynamics become the reference model outlined

in Eq. (33), implying perfect set-point tracking. By letting $\boldsymbol{\eta}(t) \triangleq \gamma(t)\mathbf{u}(t) + \boldsymbol{\theta}(t)^T \mathbf{x}(t) + \boldsymbol{\sigma}(t)$, the nominal controller can be designed as per the following:

$$\mathbf{u}_n(t) = -\boldsymbol{\eta}(t) + k_g \mathbf{r}(t) \quad (42)$$

Unfortunately, as previously stated, the parameters contained within $\boldsymbol{\eta}(t)$ are unknown, so nominal control performance cannot be achieved. Thus, the controller must make use of the estimated parameters, resulting in the final form of the control law in Eq. (43).

$$\mathbf{u}(t) = -\hat{\boldsymbol{\eta}}(t) + k_g \mathbf{r}(t) \quad (43)$$

One of the key properties of the CMAC algorithm is that the tracking error between the companion system and the plant can be shown to converge to zero as one increases adaptation rate.

$$\|\tilde{\mathbf{x}}(t)\| \leq \sqrt{\frac{\bar{\theta}_{\max}}{\lambda_{\min}(\mathbf{P})\Gamma}} \quad (44)$$

where $\lambda_{\min}(\mathbf{P})$ is the minimum eigenvalue of \mathbf{P} , and $\bar{\theta}_{\max}$ is defined by the following expression:

$$\bar{\theta}_{\max} = \max_{\theta \in \Theta} \sum_{i=1}^n 4\theta_i^2 \quad (45)$$

Note that Eq. (44) assumes zero trajectory error initialization such that $\tilde{\mathbf{x}}(0) = 0$.

C. \mathcal{L}_1 Control Architecture

In its current form, the CMAC control algorithm is an acceptable controller for systems with uncertain input gain. However, Hovakimyan and Cao [59] demonstrate that as one increases the adaptation rate Γ , the tracking performance is improved at the expense of robustness. This can be explained upon further inspection of Eqs. (39–41), where one can conclude that by increasing the magnitude of the adaptation rate Γ , the adaptive parameters become increasingly sensitive to changes in the error signal $\tilde{\mathbf{x}}(t)$. As a result, the rate of change of the control signal $\mathbf{u}(t)$ could exceed the capabilities of the plant and may drive the closed-loop system to instability.

The proposed \mathcal{L}_1 -based direct adaptive control algorithm is a relatively simple extension of the CMAC architecture that addresses this issue by applying a filtering technique that allows the performance bounds to be decoupled from the robustness of the closed-loop system. This means that the controlled system can achieve both relative fast adaptation and robustness simultaneously.

To apply this technique, let us first take the Laplace transforms of $\hat{\boldsymbol{\eta}}(t)$ to be $\hat{\boldsymbol{\eta}}(s)$, and the reference signal $\mathbf{r}(t)$ to be $\mathbf{R}(s)$. By applying a strictly proper transfer function (or low-pass filter) $D(s)$ to Eq. (43), the \mathcal{L}_1 control law is defined below:

$$U(s) = -kD(s)(\hat{\boldsymbol{\eta}}(s) - k_g \mathbf{R}(s)) \quad (46)$$

where k is a positive scalar selected by the designer. Figure 6 shows the full closed-loop system of the \mathcal{L}_1 control scheme.

Despite the simplicity of adding a low-pass filter to the control signal, there are criteria that must be met before it can be deemed \mathcal{L}_1 stable. Let us first consider the closed-loop form of the filter $D(s)$, which must yield a strictly proper, bounded-input–bounded-output (BIBO) stable transfer function

$$C(s) = \frac{k\gamma D(s)}{1 + k\gamma D(s)} \quad \forall \gamma \in \Upsilon \quad (47)$$

that has a finite gain as $s \rightarrow 0$. In order for the system to be considered \mathcal{L}_1 stable, $C(s)$ and γ must satisfy the following condition:

$$\|G(s)\|_{\mathcal{L}_1} L < 1 \quad (48)$$

where

$$L \triangleq \max_{\theta \in \Theta} \|\boldsymbol{\theta}(t)\|_1 \quad (49)$$

$$H(s) \triangleq (s\mathbb{I} - \mathbf{A}_m)^{-1} \mathbf{B} \quad (50)$$

$$G(s) \triangleq H(s)(1 - C(s)) \quad (51)$$

Now, let us consider a closed-loop reference system for the class of system outlined previously in Eq. (37) for the nonadaptive version of this controller:

$$\dot{\mathbf{x}}_{\text{ref}}(t) = \mathbf{A}_m \mathbf{x}_{\text{ref}}(t) + \mathbf{B}(\gamma(t)\mathbf{u}_{\text{ref}}(t) + \boldsymbol{\theta}(t)^T \mathbf{x}_{\text{ref}}(t) + \boldsymbol{\sigma}(t)) \quad (52)$$

$$\mathbf{U}_{\text{ref}}(s) = -\frac{C(s)}{\gamma} (\boldsymbol{\eta}_{\text{ref}}(s) - k_g \mathbf{R}(s)) \quad (53)$$

where \mathbf{x}_{ref} , $\mathbf{U}_{\text{ref}}(s)$, and $\boldsymbol{\eta}_{\text{ref}}(s)$ correspond to the closed-loop signals of \mathbf{x} , $\mathbf{U}(s)$, and $\boldsymbol{\eta}(s)$, respectively.

Theorem 2: If the selection of k and $D(s)$ verify $\|G(s)\|_{\mathcal{L}_1} L < 1$, then the closed-loop reference system in Eqs. (52) and (53) is BIBO stable with respect to $\mathbf{r}(t)$ and the initial condition \mathbf{x}_0 with guaranteed transient performance.

Proof: For the sake of brevity, please refer to the proof outlined by Zou et al. in [50], or by Hovakimyan and Cao in [59]. \square

This implies that the stability of the system greatly depends on the user's selection of the filter $D(s)$, the companion system matrices \mathbf{A}_m and \mathbf{B} , and the boundaries on the parameters $\gamma(t)$ and $\boldsymbol{\theta}(t)$. As such, these parameters cannot be arbitrarily selected, and careful consideration must be exercised when designing the \mathcal{L}_1 controller.

V. Experiments

This section covers the development and implementation of a prototype tendon-driven manipulator based on the concept highlighted in Fig. 1. This capture mechanism was used to experimentally validate the four selected control strategies: no control, PID control, indirect adaptive control, and \mathcal{L}_1 control. After performing a series of

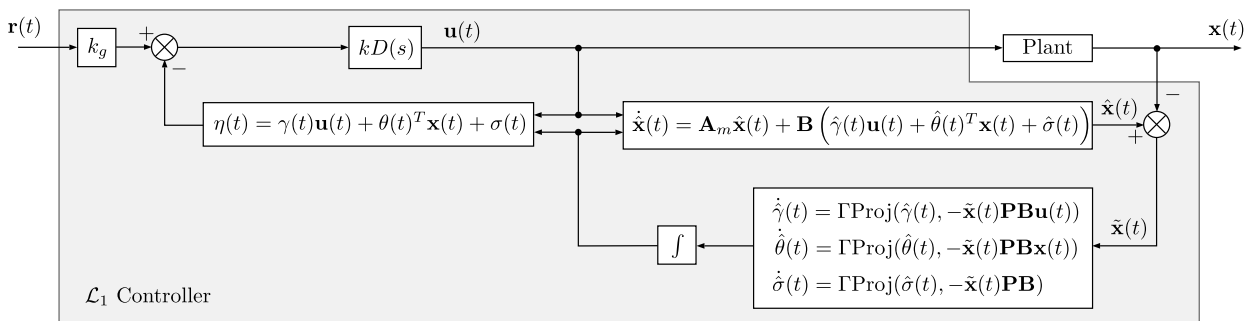


Fig. 6 \mathcal{L}_1 control architecture for systems with uncertain input gain.

maneuvers under various CSTM configurations for a single joint, the results for each control case are reported and discussed to compare their relative performance. Because this paper is isolating the performance of the controllers, the initial experiments were performed while the SPOT platform was inertially fixed.

A. SPOT Overview

One of the main objectives of the capture mechanism is that the design must perform within the capabilities of the existing facilities of the SRCL. Specifically, the capture mechanism must be compliant with the SPOT facility. There are two key components to the facility: a large gravity offset surface and an autonomous planar free-floating spacecraft analog. The platforms operate by forcing compressed air through a series of air bearings to create a near-frictionless interface on the gravity offset surface, allowing planar 3-DOF motion to emulate the free-floating nature of spacecraft.

The on-board computer is a Raspberry Pi 3 (RP3) microcomputer running a Raspbian Jessie Linux distribution as its operating system. The RP3 executes commands that drive any actuated components, on-board instruments, and data logging of the ground truth system. The manipulator must be designed to operate as the EE of the three-link manipulator while being controlled by the aforementioned on-board computer. For any further details that are not outlined in this paper pertaining to the SRCL facilities, please refer to Kernot [60], Crain [61], and Hovell [62].

1. Manipulator Assembly and Integration

The key considerations for the mechanical design of the tendon-driven gripper are as follows: the capture mechanism must interface with the wrist joint of the servo-driven three-link manipulator, the actuators driving the capture mechanism must be mounted to the base of the platform, the manipulator must be modular to allow for rapid installation/detachment from SPOT, and the contact interface of the links must be easily interchangeable. To meet these requirements, the design was selected to consist of two main components: an EE and an actuator bank. The EE was designed based on the configuration in Fig. 1 and employs rotational bearings in the joints to reduce friction. The servomotors that apply tension to the cables in the CSTM are contained within the actuator bank. This modular component houses four individual MX-28 servomotors and mounts to the base of the SPOT platforms below the shoulder joint. The arm on SPOT is driven by

The CSTM that connects the actuator bank to the EE was sourced from Asahi Intecc, Inc. The cable is a 1.07 mm PTFE coated 7×7 braided SS304 wire rope with a spherical brass ferrule, and the sheath is an SS304 flat-wire coil dimensioned as 1.2 mm \times 2.03 mm (inner diameter \times outer diameter). The tensile strength of the assembly was quoted at 300 N with a minimum bend radius of 8 mm. To attach the CSTM to the actuator bank, the sheaths are friction fitted into the four holes on the front of the U-channel such that the cable can be passed through and attached to the winch pulleys. The EE and actuator bank can be seen fully installed on the SPOT platform in Fig. 7.

2. Instrumentation and Measurements

To extract the joint angles in real time, it was deemed most appropriate to use the existing ground truth system to extract the position data of the joints from the experiment and convert them into joint angles by using the inverse kinematics of the manipulator. The primary motivations for choosing the ground truth system over other measurement systems, such as encoders, include cost effectiveness, proven reliability and accuracy from several previous experiments, simplification of the joint design, and the simplicity of physical/software implementation in the existing SPOT facilities.

The ground truth system is a PhaseSpace motion capture system. An array of eight stereoscopic cameras track the three-dimensional Cartesian coordinates of several light emitting diode (LED) markers with respect to the origin of an inertial reference frame, in this case the corner of the gravity offset table. Each LED is pulsing at a unique frequency for marker identification. This motion capture system can determine the position of an LED marker to a resolution of 0.01 mm,

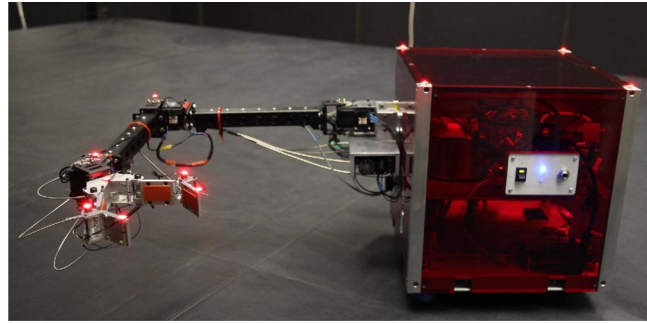


Fig. 7 Fully integrated capture mechanism on the SPOT platform.

which can be measured up to a rate of 240 Hz by the PhaseSpace server. In the case of this experiment, measurements were set to be taken at a rate of 50 Hz.

The LED configuration on the experimental hardware can be seen in Fig. 7, where there are four LEDs attached to the corners of the platform base. These LEDs are used to compute the position and attitude of the base, which is handled by the server directly. The remaining LEDs are attached to the end of each link with respect to the rotational joints.

To convert the position data of these LED markers into joint angles, the inverse kinematics of the SPOT must first be defined. The kinematic model used to derive these equations is presented in Fig. 8 for the arm and Fig. 9 for the gripper. The points marked with a dashed circle are known in the inertial reference frame from the PhaseSpace measurement system.

Note that the joint angles of the arm are measured positive-counter-clockwise and the EE joint angles are measured positive with respect to the closing direction. From geometric relationships, the joint angle of the arm and gripper can be extracted based on the knowledge of the points (x_0, y_0) to (x_{11}, y_{11}) as per the following:

$$\theta_S = \arctan\left(\frac{y_2 - y_1}{x_2 - x_1}\right) - (\pi/2 + \theta_B) \quad (54)$$

$$\theta_E = \arctan\left(\frac{y_3 - y_2}{x_3 - x_2}\right) - (\pi/2 + \theta_B + \theta_S) \quad (55)$$

$$\theta_W = \arctan\left(\frac{y_5 - y_4}{x_5 - x_4}\right) - (\pi/2 + \theta_B + \theta_S + \theta_E) \quad (56)$$

$$\theta_{LP} = -\left(\arctan\left(\frac{y_7 - y_6}{x_7 - x_6}\right) - (\pi/2 + \theta_B + \theta_S + \theta_E + \theta_W)\right) \quad (57)$$

$$\theta_{LD} = -\left(\arctan\left(\frac{y_8 - y_7}{x_8 - x_7}\right) - (\pi/2 + \theta_B + \theta_S + \theta_E - \theta_{LP} - \beta_2)\right) \quad (58)$$

$$\theta_{RP} = \arctan\left(\frac{y_{10} - y_9}{x_{10} - x_9}\right) - (\pi/2 + \theta_B + \theta_S + \theta_E + \theta_W) \quad (59)$$

$$\theta_{RD} = \arctan\left(\frac{y_{11} - y_{10}}{x_{11} - x_{10}}\right) - (\pi/2 + \theta_B + \theta_S + \theta_E + \theta_{RP} + \beta_2) \quad (60)$$

For the sake of convenience, these equations are wrapped between $-\pi < \theta < \pi$ in the software. Of the points shown, (x_1, y_1) , (x_4, y_4) , (x_6, y_6) , and (x_9, y_9) are not measured directly and must then be computed based on geometric relationships. From Figs. 8 and 9, the known parameters include $\beta_0, \beta_1, \beta_2, l_0, l_1$, and l_2 based on physical measurements. These values are recorded in Table 1.

Using these properties with reference to Eqs. (54–60), the unknown points can be found from the following equations:

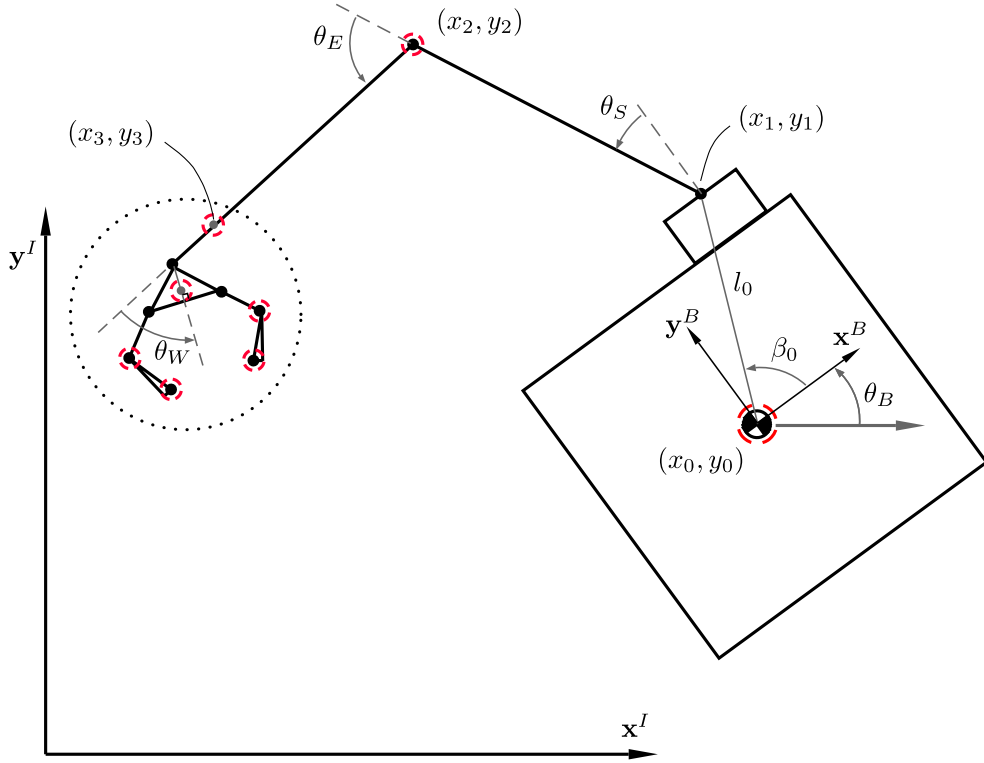


Fig. 8 Inverse kinematic model diagram of the SPOT platform with three-link manipulator.

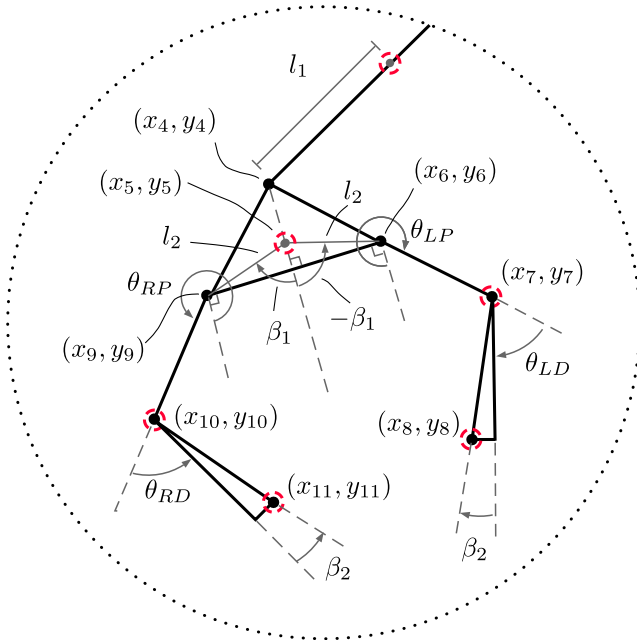


Fig. 9 Inverse kinematic model of the capture mechanism.

Table 1 List of measured geometric properties

Parameter	Value
l_0	230.4 mm
l_1	38.35 mm
l_2	34.27 mm
β_0	68.3 deg
β_1	57.0 deg
β_2	10.0 deg

$$\begin{bmatrix} x_1 \\ y_1 \end{bmatrix} = \begin{bmatrix} x_0 + l_0 \cos(\theta_B + \beta_0) \\ y_0 + l_0 \sin(\theta_B + \beta_0) \end{bmatrix} \quad (61)$$

$$\begin{bmatrix} x_4 \\ y_4 \end{bmatrix} = \begin{bmatrix} x_3 + l_1 \cos(\pi/2 + \theta_B + \theta_S + \theta_E) \\ y_3 + l_1 \sin(\pi/2 + \theta_B + \theta_S + \theta_E) \end{bmatrix} \quad (62)$$

$$\begin{bmatrix} x_6 \\ y_6 \end{bmatrix} = \begin{bmatrix} x_5 + l_2 \cos(\pi/2 + \theta_B + \theta_S + \theta_E + \beta_1) \\ y_5 + l_2 \sin(\pi/2 + \theta_B + \theta_S + \theta_E + \beta_1) \end{bmatrix} \quad (63)$$

$$\begin{bmatrix} x_9 \\ y_9 \end{bmatrix} = \begin{bmatrix} x_5 + l_2 \cos(\pi/2 + \theta_B + \theta_S + \theta_E - \beta_1) \\ y_5 + l_2 \sin(\pi/2 + \theta_B + \theta_S + \theta_E - \beta_1) \end{bmatrix} \quad (64)$$

Because Eqs. (54–60) depend on having knowledge of the preceding joint angles, they must be executed sequentially (from base to EE) to be fully defined during the experiments.

B. Experimental Results and Discussion

Here, the experimental results of the fully controlled capture mechanism are presented. Section I presents the experimental procedure and selected case studies for the various control cases. Each subsequent section is then divided into the experimental results and discussion for control case. Section II shows the performance of the uncontrolled system, Sec. III gives the performance of the baseline PID controller, the indirect adaptive controlled manipulator is given in Sec. IV, and, finally, the \mathcal{L}_1 controller is given in Sec. V.

1. Overview of Experiments

Two maneuvers were developed for the left-proximal (LP) joint of the EE: a pure sine wave maneuver (which emulates repeated opening and closing of the gripper) to capture the transient performance, and a hold maneuver with a steady-state phase. The joint angles selected for the joint of interest reflect a possible corner capture of a rectangular free-floating target, as shown in Fig. 10.

The joint parameters used for the experimental maneuvers are given in Table 2. Note that the reference trajectory is not meant to be representative of an actual capture scenario, but rather used for control performance evaluations.

These reference signals are initialized and held at $r(t) = 0$ deg for $0 \leq t \leq 20$ s to allow the ground truth system to boot and connect to the RP3 on-board the SPOT. After this duration, the reference signals are then passed to the controller blocks, where an additional internal switch controls the “ON/OFF” state of the controller. Once the controller has been activated, the transient phase of the maneuver begins, where all oscillations in the reference signal are supplied at a frequency of 5 deg/s. The purpose of the transient phase in the hold maneuver is to allow the adaptive parameters of the indirect adaptive and \mathcal{L}_1 controllers to reach a quasi-steady state before attempting the steady-state portion of the maneuver. The experiment is then terminated after 500 s, and all data are sent to the command computer for later analysis.

To fully characterize the performance of the capture mechanism under the selected control scenarios, there were several case studies performed. Aside from testing the controller’s performance with the expected operating range, it is also important to assess the controller’s performance under varying conditions of the CSTM. Thus, the experiments were performed with a straight arm configuration for the minimum friction case ($\theta_S = \theta_E = \theta_W = 0$ deg), a fully bent arm to maximize the CSTM friction ($\theta_S = \theta_E = \theta_W = 90$ deg), and a compound fully articulated dynamic friction experiment with all EE links and arm links in motion simultaneously ($0 \leq \theta \leq 90$ deg for all arm joint angles). The static arm cases were performed using the hold maneuver; the dynamic arm case used the sine wave maneuver. With the three arm configurations, two maneuvers, and four controllers, there were 12 cases run in total for five trials each to give a preliminary indication of repeatability.

2. No Control

Before analyzing the performance of the feedback controllers, the performance of the plant must first be discussed. For this scenario, the control algorithms were switched off to allow the reference signals to be passed to the plant directly. First, let us examine the performance of the LP joint in the straight arm configuration as per Fig. 11.

From the figure, it can be observed that the tracking performance of the uncontrolled plant is quite poor. The overall error reaches nearly 5 deg with an average phase delay of 2.48 s (neglecting dead zones). Furthermore, over the five trials performed, the 3σ of the standard error indicates that the plant has some stochastic elements that cause varying performance. This may be because the initial conditions vary

between trials as a result of the shut-down and star-up procedure. Despite attempts to improve its repeatability, the problem persisted, suggesting that this variance is simply the behavior of the plant.

When comparing the experimental results in Fig. 11 to the simulated plant performance for the same maneuver in Fig. 2, the general trend for the tracking error is similar. However, there is an interesting difference with the hysteresis loop. In experiment, the CSTM appears to have more prominent dead zones when a change in direction is performed, as demonstrated by the flat horizontal portions in the loop. However, the modified Bouc–Wen model has a more rounded/gradual transition into the slopes of the loop. This indicates that there is a difference between the reference model of the CSTM and the actual plant, which is to be expected. Because this is the case, it is hypothesized that the indirect indirect adaptive controller will perform worse (in general) than it would in a simulated environment because the plant does not perfectly match the model the controller was designed from. It is recognized that the parameters used in the example provided by Fig. 2 are not representative of the plant; the comparison made is simply an observation of the general behavior of the model when compared with the actual plant. Now, let us examine how the plant behaves for the same maneuver in the bent arm configuration (maximum friction) given by Fig. 12.

Immediately, one can notice that the mean trajectory is entirely above the reference signal, with a maximum error of roughly 9 deg. As the friction increases in the CSTM, the torsion spring will reach static equilibrium with the cable tension sooner than it would have in the straight arm configuration (recall that approaching a negative joint angle means that the EE is opening). This phenomenon also has an effect on the shape of the hysteresis loop. The capture mechanism becomes less responsive as the reference signal approaches -70 deg, as demonstrated by the change in width of the loop. Aside from these key differences, the overall repeatability of the tendon-driven manipulator under maximum friction conditions is similar to the repeatability in the straight arm configuration, and the average lag response is 3.848 s. Finally, the performance of the LP joint under time-varying CSTM friction is shown in Fig. 13.

In this scenario, the tracking performance of the uncontrolled plant is extremely poor, with a mean error reaching as high as 18 deg. As expected, as the arm configuration changes, so too does the shape and location of the hysteresis loop. Additionally, the signal appears to exhibit high-frequency oscillations when compared with the static case. This could be a combination of a few factors. First, the CSTM was observed to jitter during the experiment when the arm and EE were actuated simultaneously. This is likely because a change in the CSTM curvature will affect the critical point within the CSTM, ultimately determining whether the cable transmission is in a dead-zone state or a transmission state.

Furthermore, it was observed that the average trajectory of the plant fell below the reference signal, much further than the previous two arm configurations. This result at first seems peculiar because one would expect that the trajectory would fall between the minimum and maximum friction cases shown by Figs. 11 and 12, respectively. However, this phenomenon may also be a result of the cable being rapidly shifted between static and dynamic states. Because the Bouc–Wen model suggests that the form of the hysteresis loop also depends on the velocity of the tendon [Eq. (2)], a rapid change would cause the cable velocity to be greater, which would lead to a further displacement than if the arm were in a static configuration.

3. PID Control

In this section, the system performance will be analyzed under PID control for the LP joint. The gains selected for this experiment were $K_p = 0.5$, $K_i = 0.9$, and $K_d = 0.15$, which were tuned by trial and error to reduce phase delay and overshoot in the straight arm configuration. First, let us examine experimental results for the straight arm configuration shown in Fig. 14.

Indeed, the overall tracking performance of the capture mechanism is greatly improved by introducing a feedback controller into the system, where the largest error in the transient phase (excluding the drop from the initial state) was approximately 1.5 deg. Additionally,

Table 2 Description of selected reference signals

Maneuver	Steady-state θ	Transient phase
Sine wave	None	$-70 \text{ deg} \leq \theta_p \leq -45 \text{ deg}$
Hold	$\theta_p = -45 \text{ deg}$	$-70 \text{ deg} \leq \theta_p \leq -45 \text{ deg}$

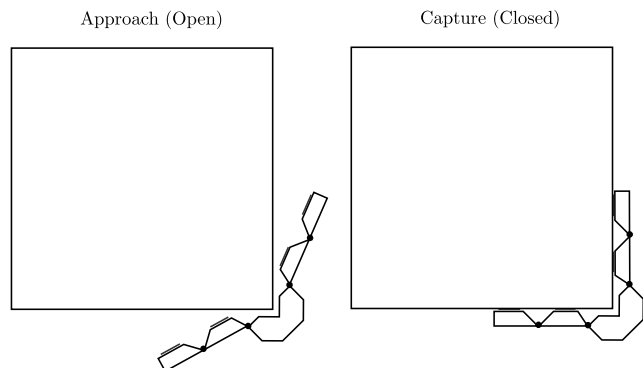


Fig. 10 Gripper configurations during the approach phase and capture phase of a free-floating SPOT platform.

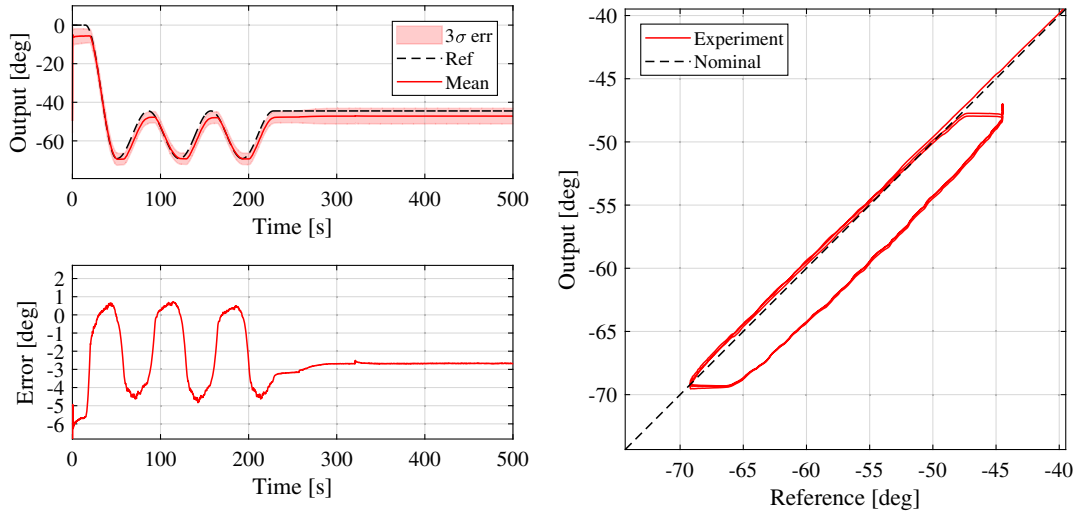


Fig. 11 LP joint tracking performance in straight arm configuration without control. Top: actual and desired proximal link angular trajectory. Bottom: mean trajectory tracking error. Right: mean hysteresis loop of transient phase.

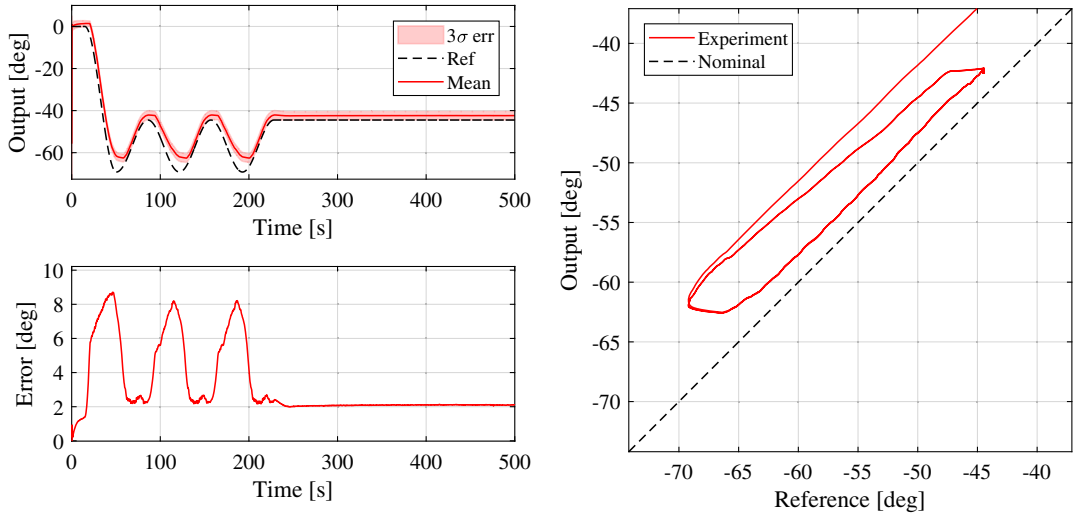


Fig. 12 LP joint tracking performance in bent arm configuration without control. Top: actual and desired proximal link angular trajectory. Bottom: mean trajectory tracking error. Right: mean hysteresis loop of transient phase.

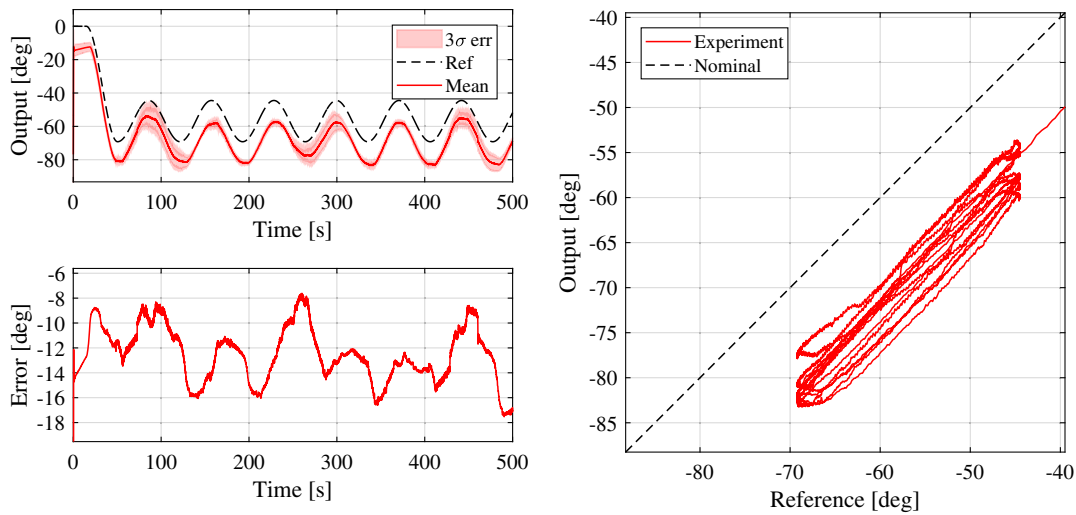


Fig. 13 LP joint tracking performance in moving arm configuration without control. Top: actual and desired proximal link angular trajectory. Bottom: mean trajectory tracking error. Right: mean hysteresis loop of transient phase.

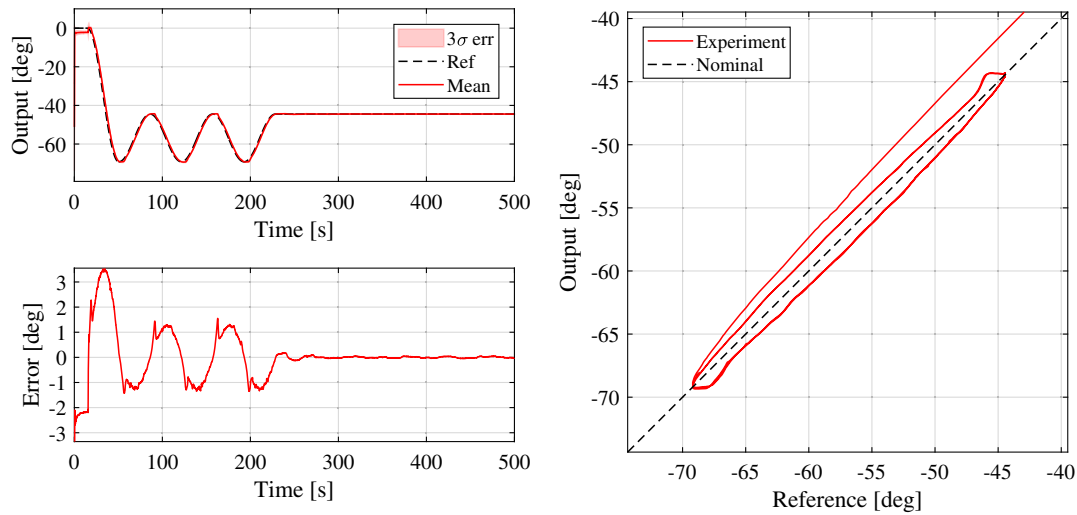


Fig. 14 LP joint tracking performance in straight arm configuration under PID control. Top: actual and desired proximal link angular trajectory. Bottom: mean trajectory tracking error. Right: mean hysteresis loop of transient phase.

the repeatability of the controlled system has improved greatly, where the 3σ error is imperceptible on the plot. With reference to the hysteresis plot, the loop is now centered on the nominal line, and the phase delay has been reduced to an average of 1.15 s. Next, the PID performance in the bent arm configuration is given by Fig. 15.

The PID controller performs nearly identically as in the straight arm configuration with a few minor differences. Upon careful inspection of the error plot, the bent arm PID case exhibits a slightly greater error in both directions, and the average lag in the response has increased to 1.22 s. This result can be justified because the fixed-gain controller must now overcome more friction to reach the reference signal. Fortunately, the integral portion of the PID controller reduces steady-state error as a result of the high transmission friction. Now, let us examine the PID controller under a dynamic arm configuration, as per Fig. 16.

Aside from the high-frequency oscillations explained previously, the overall performance is similar to the static arm cases; there is a noticeable phase delay in the system, and the transient error oscillates in a similar fashion. Note that quantifying the phase delay for the dynamic case would be nonsensical due to the presence of high-frequency oscillations. One key thing to note here is that the dead zones of the system are nearly gone, as evidenced by the absence of plateaus in the hysteresis loop. Secondly, the magnitude of the error is less consistent with time during the transient phase, ranging between roughly 1.0 and 2.0 deg. This further demonstrates that the fixed

gains of the controller produce less consistent tracking performance when subjected to variations of the plant.

4. Indirect Adaptive Control

Next, the indirect adaptive controller performance is investigated here. The controller gains selected for the experiment include $k_1 = 2$, $k_2 = 1$, $\delta_1 = \delta_2 = \delta_3 = 0.005$, $\sigma_1 = \sigma_2 = \sigma_3 = 0.01$, $\epsilon = 0.05$, and $\alpha = 1$. These gains were selected by the process outlined by Kernot [60] to reduce overshoot and phase delay. The tracking performance of the indirect adaptive controller is provided by Fig. 17 for the straight arm configuration.

Overall, the indirect adaptive controller showed excellent performance and a high degree of repeatability. Out of all the straight arm configuration cases, the indirect adaptive controller demonstrates the lowest maximum error of roughly 1.2 deg. The average phase delay in the system during this experiment was found to be 0.41 s. However, because it was previously noted that the plant differs from the Bouc–Wen model, it is to be expected that the indirect adaptive controller will have degraded performance in the presence of dynamics modeling errors. Aside from this, the indirect adaptive controller demonstrates slightly more overshoot at the transient limits when compared with the PID controller, though it maintains desirable steady-state performance. The bent arm case for the indirect adaptive controlled system is shown in Fig. 18.

As was the case with all the other controllers, the indirect adaptive performance in the bent arm case behaves similarly to its straight arm

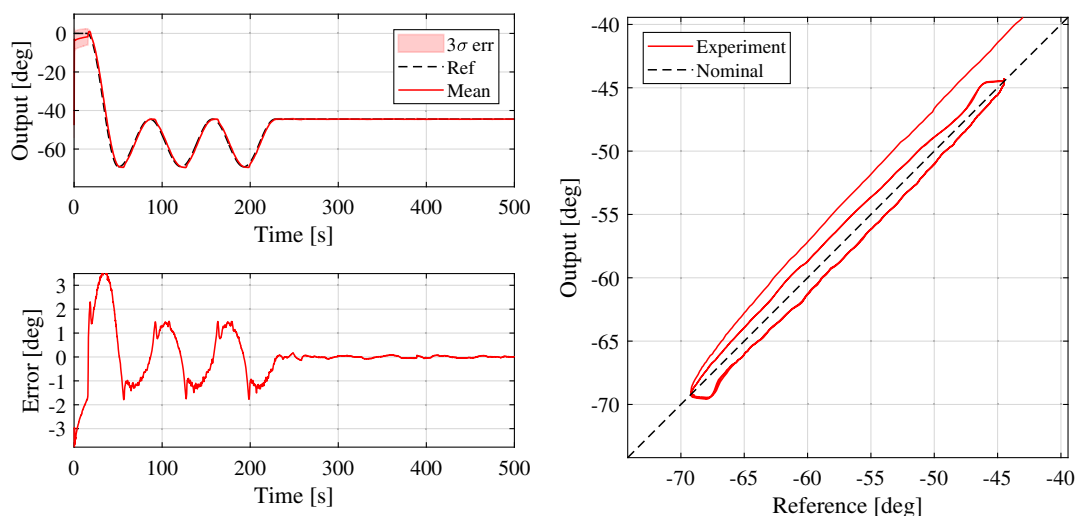


Fig. 15 LP joint tracking performance in bent arm configuration under PID control. Top: actual and desired proximal link angular trajectory. Bottom: mean trajectory tracking error. Right: mean hysteresis loop of transient phase.

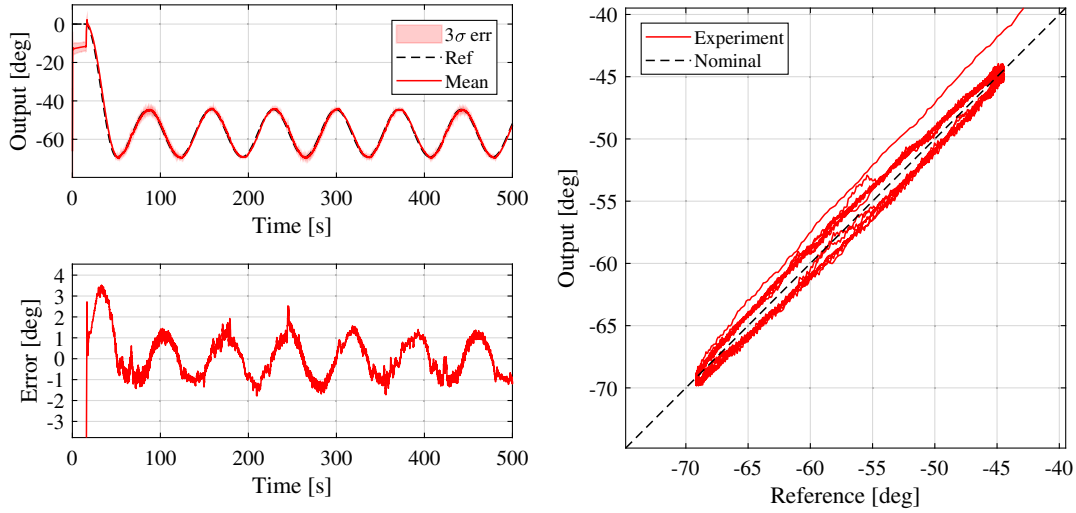


Fig. 16 LP joint tracking performance in moving arm configuration under PID control. Top: actual and desired proximal link angular trajectory. Bottom: mean trajectory tracking error. Right: mean hysteresis loop of transient phase.

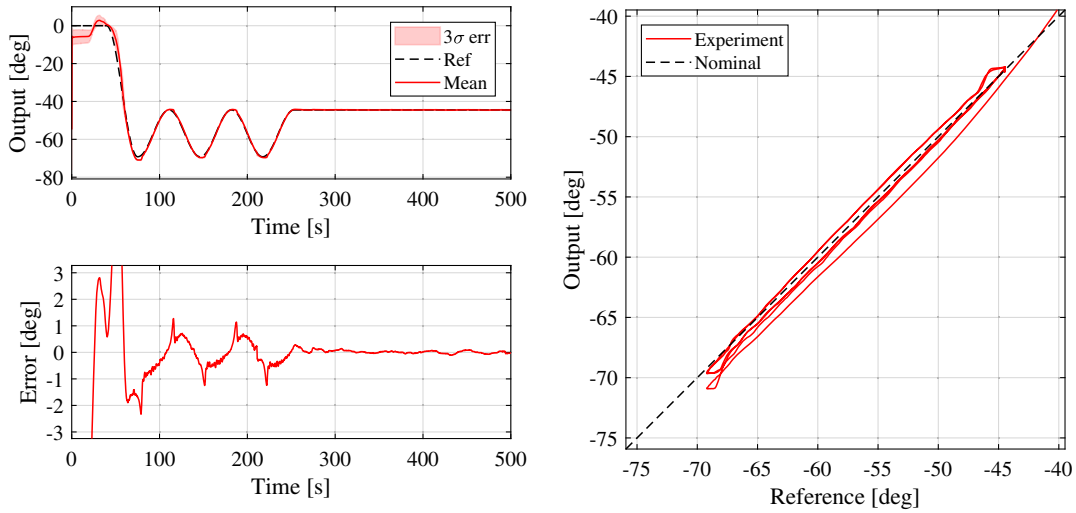


Fig. 17 LP joint tracking performance in straight arm configuration under indirect adaptive control. Top: actual and desired proximal link angular trajectory. Bottom: mean trajectory tracking error. Right: mean hysteresis loop of transient phase.

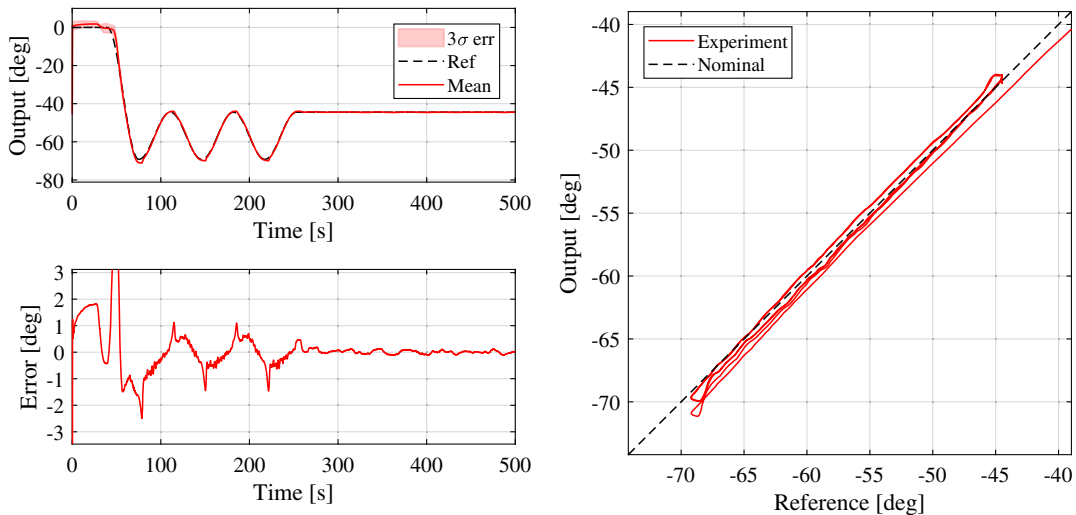


Fig. 18 LP joint tracking performance in bent arm configuration under indirect adaptive control. Top: actual and desired proximal link angular trajectory. Bottom: mean trajectory tracking error. Right: mean hysteresis loop of transient phase.

case with minor degradation. For instance, there now appear to be slight oscillations in the steady-state region, which were not observed in the straight arm case. Furthermore, the peak error has increased to approximately 1.5 deg after the learning phase, which was observed to occur over a longer period when in this arm configuration. With regard to the phase delay, there was nearly no difference from the straight arm case with the average delay being 0.40 s. Finally, the indirect adaptive controller performance during the dynamic arm maneuver is captured in Fig. 19.

As with the previous control cases, the dead zones have been eliminated, high-frequency oscillations have been introduced, and the repeatability has been degraded. With reference to the error plot, the magnitude of the error remained consistent with respect to the other arm configurations. Similarly, a comparable phase delay can be observed on the hysteresis plot, which suggests that this is an artifact of the experimental plant not matching the Bouc–Wen model exactly. Overall, the indirect adaptive controller demonstrates a higher degree of consistency between its static and dynamic arm configurations when compared with the other controllers, implying that it may be the most reliable.

5. \mathcal{L}_1 Control

Finally, the performance of the \mathcal{L}_1 -controlled LP joint is analyzed here. The controller parameters chosen for the experiment were $\Gamma = 2.5$, $k = 1$, $t_s = 2$, and $\psi = 1/9$ to reduce overshoot and phase delay. The low pass filter used in experiment was $D(s) = 1/s$, as it is commonly used, and it provides a more simple case for these first-order experiments. Because this is the first experiment with the \mathcal{L}_1 controller used on the SPOT platform, the filter design was intentionally left simplistic to reduce the amount of variables to tune in the real system. Future work could indeed involve a more complex filter design; however, this cannot be realized for this particular paper. For the selected gains, the \mathcal{L}_1 stability condition was met with $\|G(s)\|_{\mathcal{L}_1} L = 0.9091$, as per Eq. (48). In theory, the Γ gain can be set arbitrarily high, with no consequences on the system; however, this could not be realized in the real system. The command signals occasionally saturated safety constraints on the hardware and led to control issues. Furthermore, the low magnitude Γ gain was justified because the objective of implementing the \mathcal{L}_1 control strategy for the SPOT gripper system was not to explore the features of \mathcal{L}_1 to achieve the theoretical performance guarantees established by \mathcal{L}_1 theory, but instead designing an \mathcal{L}_1 control law capable of managing the non-linear hysteresis while providing satisfactory trajectory tracking performance in the context of our experimental testbed. As is shown by the following results, the current selection of design parameters does indeed satisfy the performance requirements and the stability criteria, even with a low gamma value, thereby alleviating the need

for further tuning. Additionally, due to the large time scale of the experiment, the low Γ gain shows the transient phase of the controller adaptation more clearly.

The performance of the \mathcal{L}_1 controlled LP joint is shown in Fig. 20 for the straight arm configuration. Note that there is an initially high error near the beginning of the experiment during the learning phase of the controller, which is in disagreement with the conditions necessary for Eq. (44). The software controlling the experiment was set to initialize the system to zero trajectory error; however, various unmodeled dynamic effects in the physical hardware affected the initialization of the experiment and an initial zero trajectory error could not be avoided.

Once again, the performance of the system was improved, with the 3σ error being negligible in terms of repeatability. An interesting aspect to note is that the adaptive parameters for the \mathcal{L}_1 controller have a faster convergence time as compared with the indirect adaptive controller, as demonstrated by the learning phase near the start of the experiment. Moreover, the average error was reduced, and phase lag in the system was found to be 0.32 s.

Despite the overall phase and error improvements, the hysteresis loop shows that there is a greater overshoot, specifically at the limits of the transient wave compared with the PID and indirect adaptive controlled cases (i.e., the output extends past the -70 deg mark). The overshoot is quite small, though it is worth noting because overshoot is undesirable in robotic applications. Furthermore, the \mathcal{L}_1 controller appears to give an oscillatory response in steady state, which was not exhibited in the previous control cases. It is difficult to determine the exact cause of this phenomenon because there are several gain parameters, though it is suspected that the filter could be optimized further to improve the results. Now, the tracking performance for the bent arm configuration in Fig. 21 will be investigated.

When compared with the straight arm configuration, the bent arm case exhibited similar performance with only minor differences. In this case, the phase delay was slightly higher than the straight arm case with a value of 0.39 s; this is expected because there is more friction introduced to the system. Secondly, the overall error throughout the experiment was higher in general. That is to say, the peak error reached was roughly 2 deg, and the magnitude of the steady-state oscillations has increased. What is most interesting about the \mathcal{L}_1 controller is its performance during the dynamic arm configuration, presented in Fig. 22.

Overall, the average error is less than what was observed during the transient phases of the preceding arm configurations, where the error stays roughly under 1.2 deg throughout the experiment. This is likely because the dead zones have been reduced (as was observed in the previous dynamic arm cases), because dead-zone performance was in fact the main source of error in the static arm cases. The phase delay in this case was imperceptible due to the high-frequency oscillations

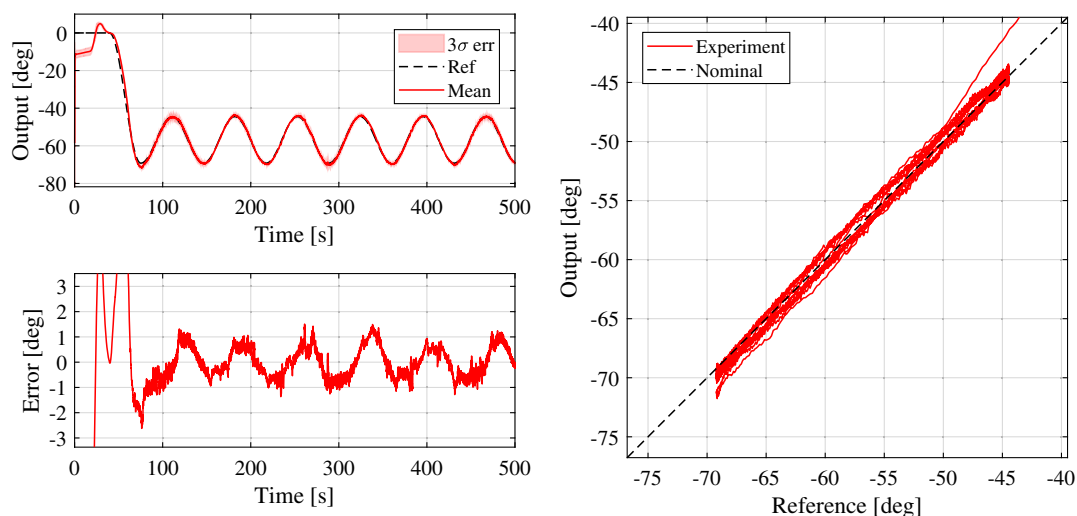


Fig. 19 LP joint tracking performance in moving arm configuration under indirect adaptive control. Top: actual and desired proximal link angular trajectory. Bottom: mean trajectory tracking error. Right: mean hysteresis loop of transient phase.

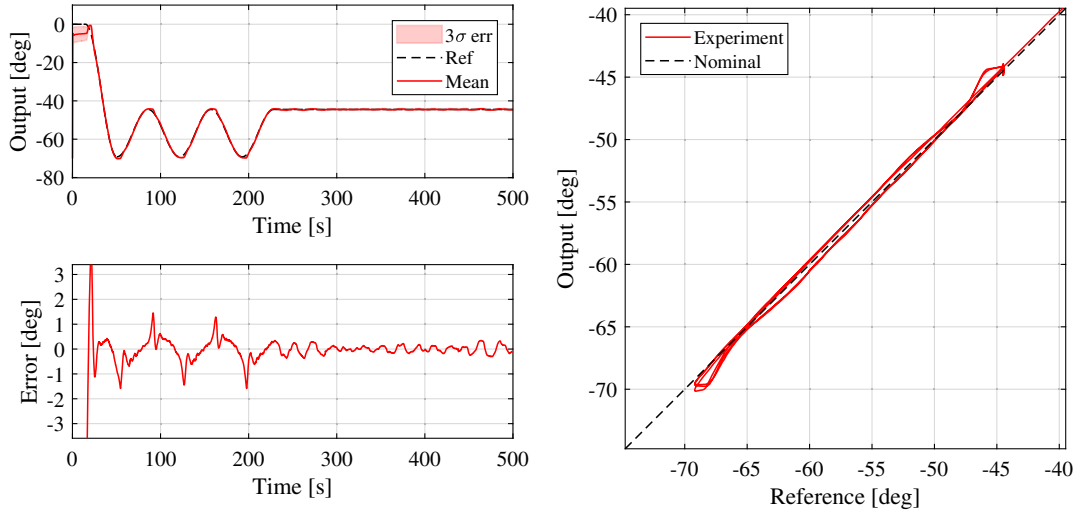


Fig. 20 LP joint tracking performance in straight arm configuration under \mathcal{L}_1 control. Top: actual and desired proximal link angular trajectory. Bottom: mean trajectory tracking error. Right: mean hysteresis loop of transient phase.

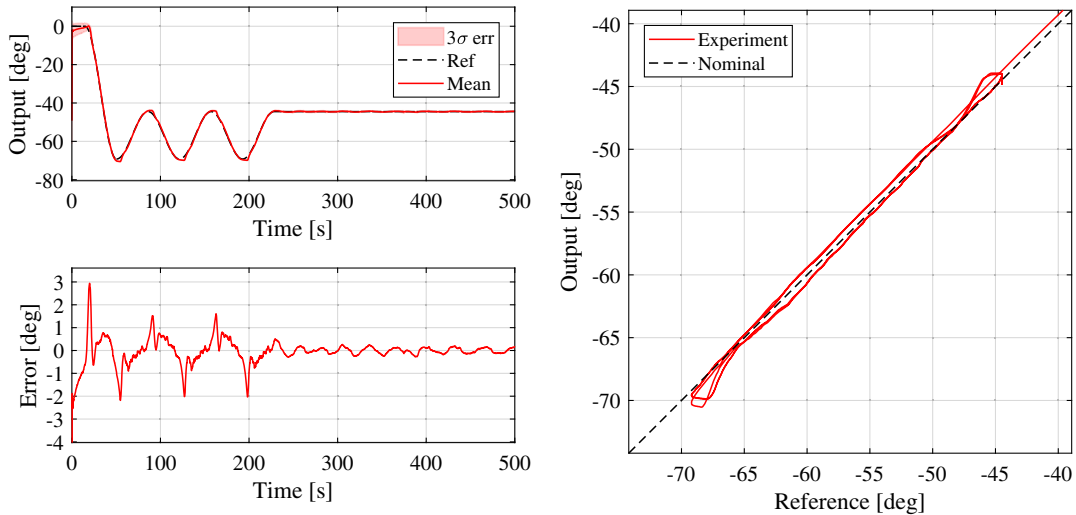


Fig. 21 LP joint tracking performance in bent arm configuration under \mathcal{L}_1 control. Top: actual and desired proximal link angular trajectory. Bottom: mean trajectory tracking error. Right: mean hysteresis loop of transient phase.

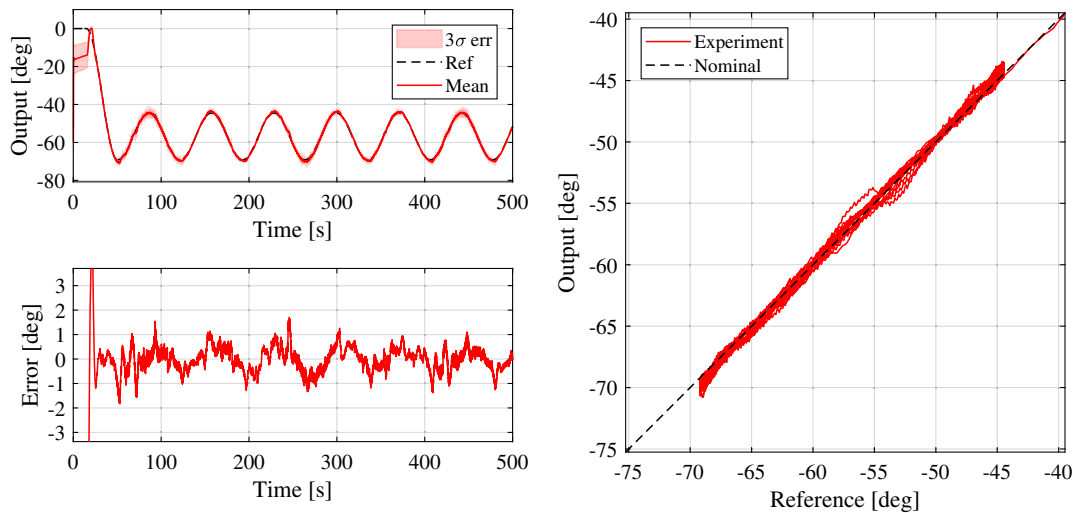


Fig. 22 LP joint tracking performance in moving arm configuration under \mathcal{L}_1 control. Top: actual and desired proximal link angular trajectory. Bottom: mean trajectory tracking error. Right: mean hysteresis loop of transient phase.

in the data. From the results obtained, it can be said that the \mathcal{L}_1 controller has the best performance under dynamic reference signals and arm configurations, whereas the indirect adaptive controller performs best during a hold maneuver while the CSTM is in a static state. This implies that the \mathcal{L}_1 controller has the best performance when subjected to plant variations and unmodeled dynamics.

VI. Conclusions

In this paper, the adaptive control of the prototype tendon-driven capture mechanism was investigated. Specifically, the control algorithms employed include a well-performing indirect control algorithm and a direct \mathcal{L}_1 control law that have never before been applied to a multilink manipulator actuated via cable-sheath transmission mechanism. The performance of these controllers was compared against the baseline open-loop and proportional-integral-derivative controlled cases experimentally. Although the indirect adaptive controller still demonstrated the best tracking performance in terms of minimizing the overall tracking, overshoot, and steady-state error, the \mathcal{L}_1 performed only slightly worse in these aspects while maintaining a better transient response by reducing the phase delay to nearly zero. From the results obtained, one can draw the conclusion that the \mathcal{L}_1 controller performs best in dynamic arm configurations, whereas the indirect adaptive controller performs best during a hold maneuver while the cable-sheath transmission mechanism is in a static state.

With regard to the practicality of implementing the adaptive control laws presented to a cable-sheath transmission mechanism, however, it was shown that both solutions have their advantages and limitations when implemented into a physical system. When introduced to a different tendon-driven manipulator that uses a cable-sheath transmission mechanism, there is a possibility that there is a clear distinction for which controller performs best. Additionally, the performances of these controllers may be suboptimal because the tuning performed was based on qualitative tuning methods to the best of the authors' ability.

References

- [1] Kelso, T. S., "Celestrak SATCAT Boxscore Database," March 2018, <https://www.celestrak.com/satcat/search.php> [retrieved 15 March 2018].
- [2] Kessler, D. J., and Cour-Palais, B. G., "Collision Frequency of Artificial Satellites: The Creation of a Debris Belt," *Journal of Geophysical Research: Space Physics*, Vol. 83, No. A6, 1978, pp. 2637–2646. <https://doi.org/10.1029/JA083iA06p02637>
- [3] Liou, J.-C., and Johnson, N. L., "Instability of the Present LEO Satellite Populations," *Advances in Space Research*, Vol. 41, No. 7, 2008, pp. 1046–1053. <https://doi.org/10.1016/j.asr.2007.04.081>
- [4] Schaub, H., Jasper, L. E. Z., Anderson, P. V., and McKnight, D. S., "Cost and Risk Assessment for Spacecraft Operation Decisions Caused by the Space Debris Environment," *Acta Astronautica*, Vol. 113, Aug. 2015, pp. 66–79. <https://doi.org/10.1016/j.actaastro.2015.03.028>
- [5] Kessler, D. J., Johnson, N. L., Liou, J., and Matney, M., "The Kessler Syndrome: Implications to Future Space Operations," *Advances in the Astronautical Sciences*, Vol. 137, No. 8, 2010, p. 2010.
- [6] Shan, M., Guo, J., and Gill, E., "Review and Comparison of Active Space Debris Capturing and Removal Methods," *Progress in Aerospace Sciences*, Vol. 80, Jan. 2016, pp. 18–32. <https://doi.org/10.1016/j.paerosci.2015.11.001>
- [7] Wormnes, K., Le Letty, R., Summerer, L., Schonenborg, R., Dubois-Matra, O., Luraschi, E., Cropp, A., Krag, H., and Delaval, J., "ESA Technologies for Space Debris Remediation," *6th European Conference on Space Debris*, Vol. 1, ESA Communications ESTEC, Noordwijk, The Netherlands, 2013, pp. 1–8.
- [8] Oda, M., Kibe, K., and Yamagata, F., "ETS-VII, Space Robot In-Orbit Experiment Satellite," *Proceedings of IEEE International Conference on Robotics and Automation*, Vol. 1, Inst. of Electrical and Electronics Engineers, New York, 1996, pp. 739–744. <https://doi.org/10.1109/ROBOT.1996.503862>
- [9] Jorgensen, G., and Bains, E., "SRMS History, Evolution and Lessons Learned," *AIAA SPACE 2011 Conference & Exposition*, AIAA Paper 2011-7277, 2011. <https://doi.org/10.2514/6.2011-7277>
- [10] Ticker, R. L., Cepollina, F., and Reed, B. B., "NASA's In-Space Robotic Servicing," *AIAA SPACE 2015 Conference and Exposition*, AIAA Paper 2015-4644, 2015. <https://doi.org/10.2514/6.2015-4644>
- [11] Romano, M., Friedman, D. A., and Shay, T. J., "Laboratory Experimentation of Autonomous Spacecraft Approach and Docking to a Collaborative Target," *Journal of Spacecraft and Rockets*, Vol. 44, No. 1, 2007, pp. 164–173. <https://doi.org/10.2514/1.22092>
- [12] Pinson, R., Howard, R., and Heaton, A., "Orbital Express Advanced Video Guidance Sensor: Ground Testing, Flight Results and Comparisons," *AIAA Guidance, Navigation and Control Conference and Exhibit*, AIAA Paper 2008-7318, 2008. <https://doi.org/10.2514/6.2008-7318>
- [13] Medina, A., Tomassini, A., Suatoni, M., Avilés, M., Solway, N., Coxhill, I., Paraskevas, I. S., Rekleitis, G., Papadopoulos, E., Krenn, R., Brito, A., Sabbatinelli, B., Wollenhaupt, B., Vidal, C., Aziz, S., and Gianfranco, V., "Towards a Standardized Grasping and Refuelling On-Orbit Servicing for Geo Spacecraft," *Acta Astronautica*, Vol. 134, May 2017, pp. 1–10. <https://doi.org/10.1016/j.actaastro.2017.01.022>
- [14] Virgili-Llop, J., Drew, J. V., Zappulla, R., II, and Romano, M., "Laboratory Experiments of Resident Space Object Capture by a Spacecraft-Manipulator System," *Aerospace Science and Technology*, Vol. 71, Dec. 2017, pp. 530–545. <https://doi.org/10.1016/j.ast.2017.09.043>
- [15] Benavides, J. V., and Bualat, M. G., "SPHERES: Synchronized, Position, Hold, Engage, Reorient, Experimental Satellites," NASA Technical Reports Server, 2018, <https://ntrs.nasa.gov/citations/20180007934>.
- [16] Henshaw, C. G., "The Darpa Phoenix Spacecraft Servicing Program: Overview and Plans for Risk Reduction," *International Symposium on Artificial Intelligence, Robotics and Automation in Space (i-SAIRAS)*, European Space Agency, 2014, Paper 43.
- [17] Debus, T., and Dougherty, S., "Overview and Performance of the Front-End Robotics Enabling Near-Term Demonstration (FRIEND) Robotic Arm," *AIAA Infotech@Aerospace Conference and AIAA Unmanned . . . Unlimited Conference*, AIAA Paper 2009-1870, 2009. <https://doi.org/10.2514/6.2009-1870>
- [18] Wieser, M., Richard, H., Hausmann, G., Meyer, J.-C., Jaekel, S., Lavagna, M., and Biesbroek, R., "E. Deorbit Mission: OHB Debris Removal Concepts," *13th Symposium on Advanced Space Technologies in Robotics and Automation (ASTRA)*, European Space Agency, 2015, Paper 100732.
- [19] Ratti, J., "Launch Adapter Ring (LAR) Capture Tool: Enabling Space Robotic Servicing," *Proceedings of International Conference on Robotics and Automation, Workshop on The Next Generation of Space Robotic Servicing Technologies*, IEEE, New York, 2015.
- [20] Jaworski, J., Dudek, E., Wolski, M., Mateja, A., Wittels, P., Łabecki, M., Dellandréa, B., Christy, J., Dubanchet, V., and Le Peuvedic, C., "Grippers for Capture Launch Adapter Rings of Non-Cooperative Satellites for Active Debris Removal, Space Tug and On-Orbit Satellite Servicing Applications," *Proceedings of 14th Symposium on Advanced Space Technologies in Robotics and Automation (ASTRA'2017)*, European Space Agency, 2017, Paper S2A16.20.
- [21] Oleś, J., Rybus, T., Seweryn, K., Surowiec, M., Wojtyra, M., Pietras, M., and Scheper, M., "Testing and Simulation of Contact During On-Orbit Operations," *Proceedings of 14th Symposium on Advanced Space Technologies in Robotics and Automation (ASTRA'2017)*, European Space Agency, 2017, Paper SB514.25.
- [22] Richard, M., Kronig, L., Belloni, F., Rossi, S., Gass, V., Paccolat, C., Thiran, J., Araomi, S., Gavrilovich, I., and Shea, H., "Uncooperative Rendezvous and Docking for MicroSats," *6th International Conference on Recent Advances in Space Technologies*, Turkish Air Force Academy, 2013.
- [23] Ozawa, R., Kobayashi, H., and Hashiri, K., "Analysis, Classification, and Design of Tendon-Driven Mechanisms," *IEEE Transactions on Robotics*, Vol. 30, No. 2, 2014, pp. 396–410. <https://doi.org/10.1109/TRO.2013.2287976>
- [24] Ma, S., Hirose, S., and Yoshinada, H., "Design and Experiments for a Coupled Tendon-Driven Manipulator," *IEEE Control Systems Magazine*, Vol. 13, No. 1, 1993, pp. 30–36. <https://doi.org/10.1109/37.184790>
- [25] Le, H. M., Do, T. N., and Phee, S. J., "A Survey on Actuators-Driven Surgical Robots," *Sensors and Actuators A: Physical*, Vol. 247, Aug. 2016, pp. 323–354. <https://doi.org/10.1016/j.sna.2016.06.010>
- [26] Li, K., Zhang, Y., and Hu, Q., "Dynamic Modelling and Control of a Tendon-Actuated Lightweight Space Manipulator," *Aerospace Science and Technology*, Vol. 84, Jan. 2019, pp. 1150–1163. <https://doi.org/10.1016/j.ast.2018.11.018>

- [27] Tsai, L.-W., "Design of Tendon-Driven Manipulators," *Journal of Mechanical Design*, Vol. 117, 1995, pp. 80–86.
<https://doi.org/10.1115/1.2836474>
- [28] Kobayashi, H., Hyodo, K., and Ogane, D., "On Tendon-Driven Robotic Mechanisms with Redundant Tendons," *International Journal of Robotics Research*, Vol. 17, No. 5, 1998, pp. 561–571.
<https://doi.org/10.1177/027836499801700507>
- [29] Fuxiang, T., and Xingsong, W., "The Design of a Tendon-Sheath-Driven Robot," *2008 15th International Conference on Mechatronics and Machine Vision in Practice*, Inst. of Electrical and Electronics Engineers, New York, 2008, pp. 280–284.
<https://doi.org/10.1109/MMVIP.2008.4749547>
- [30] Lin, C., Xingsong, W., and Fuxiang, T., "Tendon-Sheath Actuated Robots and Transmission System," *International Conference on Mechatronics and Automation, 2009, ICMA 2009*, Inst. of Electrical and Electronics Engineers, New York, 2009, pp. 3173–3178.
<https://doi.org/10.1109/ICMA.2009.5246171>
- [31] Kaneko, M., Yamashita, T., and Tanie, K., "Basic Considerations on Transmission Characteristics for Tendon Drive Robots," *Fifth International Conference on Advanced Robotics, 1991: Robots in Unstructured Environments, 91 ICAR*, Inst. of Electrical and Electronics Engineers, New York, 1991, pp. 827–832.
<https://doi.org/10.1109/ICAR.1991.240572>
- [32] Kaneko, M., Wada, M., Maekawa, H., and Tanie, K., "A New Consideration on Tendon-Tension Control System of Robot Hands," *Proceedings of 1991 IEEE International Conference on Robotics and Automation*, Inst. of Electrical and Electronics Engineers, New York, 1991, pp. 1028–1033.
<https://doi.org/10.1109/ROBOT.1991.131727>
- [33] Palli, G., and Melchiorri, C., "Model and Control of Tendon-Sheath Transmission Systems," *Proceedings of 2006 IEEE International Conference on Robotics and Automation, 2006, ICRA 2006*, Inst. of Electrical and Electronics Engineers, New York, 2006, pp. 988–993.
<https://doi.org/10.1109/ROBOT.2006.1641838>
- [34] Palli, G., Borghesan, G., and Melchiorri, C., "Tendon-Based Transmission Systems for Robotic Devices: Models and Control Algorithms," *IEEE International Conference on Robotics and Automation, 2009, ICRA '09*, Inst. of Electrical and Electronics Engineers, New York, 2009, pp. 4063–4068.
<https://doi.org/10.1109/ROBOT.2009.5152491>
- [35] Palli, G., and Melchiorri, C., "Optimal Control of Tendon-Sheath Transmission Systems," *IFAC Proceedings Volumes*, Vol. 39, No. 15, 2006, pp. 73–78.
<https://doi.org/10.3182/20060906-3-IT-2910.00014>
- [36] Agrawal, V., Peine, W. J., Yao, B., and Choi, S., "Control of Cable Actuated Devices Using Smooth Backlash Inverse," *2010 IEEE International Conference on Robotics and Automation (ICRA)*, Inst. of Electrical and Electronics Engineers, New York, 2010, pp. 1074–1079.
<https://doi.org/10.1109/ROBOT.2010.5509533>
- [37] Kesner, S. B., and Howe, R. D., "Position Control of Motion Compensation Cardiac Catheters," *IEEE Transactions on Robotics*, Vol. 27, No. 6, 2011, pp. 1045–1055.
<https://doi.org/10.1109/TRO.2011.2160467>
- [38] Reilink, R., Stramigioli, S., and Misra, S., "Image-Based Hysteresis Reduction for the Control of Flexible Endoscopic Instruments," *Mechatronics*, Vol. 23, No. 6, 2013, pp. 652–658.
<https://doi.org/10.1016/j.mechatronics.2013.06.006>
- [39] Xu, K., and Simaan, N., "Actuation Compensation for Flexible Surgical Snake-Like Robots with Redundant Remote Actuation," *Proceedings of 2006 IEEE International Conference on Robotics and Automation, 2006, ICRA 2006*, Inst. of Electrical and Electronics Engineers, New York, 2006, pp. 4148–4154.
<https://doi.org/10.1109/ROBOT.2006.1642340>
- [40] Xu, K., Zhao, J., and Fu, M., "Development of the SJTU Unfoldable Robotic System (SURS) for Single Port Laparoscopy," *IEEE/ASME Transactions on Mechatronics*, Vol. 20, No. 5, 2015, pp. 2133–2145.
<https://doi.org/10.1109/TMECH.2014.2364625>
- [41] Xu, K., and Simaan, N., "An Investigation of the Intrinsic Force Sensing Capabilities of Continuum Robots," *IEEE Transactions on Robotics*, Vol. 24, No. 3, 2008, pp. 576–587.
<https://doi.org/10.1109/TRO.2008.924266>
- [42] Wang, X.-S., Su, C.-Y., and Hong, H., "Robust Adaptive Control of a Class of Nonlinear Systems with Unknown Dead-Zone," *Automatica*, Vol. 40, No. 3, 2004, pp. 407–413.
<https://doi.org/10.1016/j.automatica.2003.10.021>
- [43] Guo, J., Wang, F., and Yao, B., "Adaptive Control for Nonlinear System with Unknown Hysteresis," *2012 24th Chinese Control and Decision Conference (CCDC)*, Inst. of Electrical and Electronics Engineers, New York, 2012, pp. 1067–1072.
<https://doi.org/10.1109/CCDC.2012.6244169>
- [44] Hu, C., Yao, B., and Wang, Q., "Performance-Oriented Adaptive Robust Control of a Class of Nonlinear Systems Preceded by Unknown Dead Zone with Comparative Experimental Results," *IEEE/ASME Transactions on Mechatronics*, Vol. 18, No. 1, 2011, pp. 178–189.
<https://doi.org/10.1109/TMECH.2011.2162633>
- [45] Tao, G., and Kokotovic, P. V., "Adaptive Control of Plants with Unknown Dead-Zones," *IEEE Transactions on Automatic Control*, Vol. 39, No. 1, 1994, pp. 59–68.
<https://doi.org/10.1109/9.273339>
- [46] Do, T., Tjahjowidodo, T., Lau, M., Yamamoto, T., and Phee, S., "Hysteresis Modeling and Position Control of Tendon-Sheath Mechanism in Flexible Endoscopic Systems," *Mechatronics*, Vol. 24, No. 1, 2014, pp. 12–22.
<https://doi.org/10.1016/j.mechatronics.2013.11.003>
- [47] Do, T. N., Tjahjowidodo, T., Lau, M. W. S., and Phee, S. J., "Enhanced Performances for Cable-Driven Flexible Robotic Systems with Asymmetric Backlash Profile," *2015 IEEE International Conference on Technologies for Practical Robot Applications (TePRA)*, Inst. of Electrical and Electronics Engineers, New York, 2015, pp. 1–6.
<https://doi.org/10.1109/TePRA.2015.7219674>
- [48] Do, T. N., Tjahjowidodo, T., Lau, M. W. S., and Phee, S. J., "Position Control of Asymmetric Nonlinearities for a Cable-Conduit Mechanism," *IEEE Transactions on Automation Science and Engineering*, Vol. 14, No. 3, 2017, pp. 1515–1523.
<https://doi.org/10.1109/TASE.2015.2438319>
- [49] Kaufman, H., Barkana, I., and Sobel, K., *Direct Adaptive Control Algorithms: Theory and Applications*, 2nd ed., Communications and Control Engineering Series, Springer, New York, 1997, pp. 42–45.
<https://doi.org/10.1007/978-1-4612-0657-6>
- [50] Zou, X., Cao, C., and Hovakimyan, N., "L1 Adaptive Controller for Systems with Hysteresis Uncertainties," *Proceedings of the 2010 American Control Conference*, Inst. of Electrical and Electronics Engineers, New York, 2010, pp. 6662–6667.
<https://doi.org/10.1109/ACC.2010.5531361>
- [51] Fan, X., and Smith, R. C., "L1 Adaptive Control of Hysteresis in Smart Materials," *Modeling, Signal Processing, and Control for Smart Structures 2008*, Vol. 6926, International Soc. for Optics and Photonics, Society of Photo-Optical Instrumentation Engineers (SPIE), Bellingham, WA, 2008, Paper 69260G.
<https://doi.org/10.1117/12.779316>
- [52] Zhang, J., Yang, Q., and Zhou, C., "L1 Adaptive Control Design for Hysteresis Compensation within Piezoelectric Actuators," *IFAC Proceedings Volumes*, Vol. 47, No. 3, 2014, pp. 2691–2696.
<https://doi.org/10.3182/20140824-6-ZA-1003.02659>
- [53] Yousef, H. A., Hamdy, M., and Nashed, K., "L1 Adaptive Fuzzy Controller for a Class of Nonlinear Systems with Unknown Backlash-Like Hysteresis," *International Journal of Systems Science*, Vol. 48, No. 12, 2017, pp. 2522–2533.
<https://doi.org/10.1080/00207721.2017.1324065>
- [54] Palli, G., "Model and Control of Tendon Actuated Robots," Ph.D. Thesis, Alma Mater Studiorum Univ. di Bologna, Bologna, Italy, 2007. <https://doi.org/10.6092/unibo/amsdottorato/341>
- [55] Song, J., and Der Kiureghian, A., "Generalized Bouc–Wen Model for Highly Asymmetric Hysteresis," *Journal of Engineering Mechanics*, Vol. 132, No. 6, 2006, pp. 610–618.
[https://doi.org/10.1061/\(ASCE\)0733-9399\(2006\)132:6\(610\)](https://doi.org/10.1061/(ASCE)0733-9399(2006)132:6(610))
- [56] Dodenhöft, J., Choe, R., Ackerman, K., Holzapfel, F., and Hovakimyan, N., "Design and Evaluation of an L1 Adaptive Controller for NASA's Transport Class Model," *AIAA Guidance, Navigation, and Control Conference*, AIAA Paper 2017-1250, 2017.
<https://doi.org/10.2514/6.2017-1250>
- [57] Jafarnejadsani, H., Lee, H., and Hovakimyan, N., "L1 Adaptive Sampled-Data Control for Uncertain Multi-Input Multi-Output Systems," *Automatica*, Vol. 103, May 2019, pp. 346–353.
<https://doi.org/10.1016/j.automatica.2019.01.007>
- [58] Nayyeri, P., Mohammadi, A., and Zakerzadeh, M. R., "Optimal-Tuned Parameters for L1 Adaptive Control," *2019 7th International Conference on Robotics and Mechatronics (ICRoM)*, Inst. of Electrical and Electronics Engineers, New York, 2019, pp. 13–16.
<https://doi.org/10.1109/ICRoM48714.2019.9071843>
- [59] Hovakimyan, N., and Cao, C., *L1 Adaptive Control Theory: Guaranteed Robustness with fast adaptation*, Vol. 21, Soc. for Industrial and Applied Mathematics, University City, PA, 2010, Chaps. 4, 5.
<https://doi.org/10.1137/1.9780898719376>
- [60] Kernot, J., "Design and Adaptive Control of a Tendon-Driven Manipulator for the Capture of Non-Cooperative Space Targets," Master's

- Thesis, Carleton Univ., Ottawa, 2019.
<https://doi.org/10.22215/etd/2019-13643>
- [61] Crain, A., "Optimal Trajectory Planning and Compliant Spacecraft Capture Using a Space Robot," Master's Thesis, Carleton Univ., Ottawa, 2018.
<https://doi.org/10.22215/etd/2018-12971>
- [62] Hovell, K., "Detumbling Space Debris Using Tethers," Master's Thesis, Carleton Univ., Ottawa, 2017.
<https://doi.org/10.22215/etd/2017-11870>

M. A. Ayoubi
Associate Editor